

First Space-Based Microlens Parallax Measurement: *Spitzer* Observations of OGLE-2005-SMC-001

S. Dong^{1,2}, A. Udalski^{3,4}, A. Gould^{1,2}, W.T. Reach⁵, G.W. Christie^{2,6}, A.F. Boden^{7,8},
D.P. Bennett⁹, G. Fazio¹⁰, K. Griest¹¹, M.K. Szymański^{3,4}, M. Kubiak^{3,4}, I. Soszyński^{3,4},
G. Pietrzyński^{3,4,12}, O. Szewczyk^{3,4}, L. Wyrzykowski^{3,4,13}, K. Ulaczyk^{3,4}, T. Wieckowski^{3,4},
B. Paczyński^{3,14}, D.L. DePoy^{1,2}, R.W. Pogge^{1,2}, G.W. Preston¹⁵, I.B. Thompson¹⁵

ABSTRACT

We combine *Spitzer* and ground-based observations to measure the microlens parallax of OGLE-2005-SMC-001, the first space-based such determination since Refsdal proposed the idea in 1966. The parallax measurement yields a projected

¹Department of Astronomy, Ohio State University, 140 W. 18th Ave., Columbus, OH 43210, USA; depoy,dong,gould,pogge@astronomy.ohio-state.edu

²Microlensing Follow Up Network (μ FUN)

³Optical Gravitational Lens Experiment (OGLE)

⁴Warsaw University Observatory, Al. Ujazdowskie 4, 00-478 Warszawa, Poland; udalski,msz,mk,soszynsk,pietrzyn,szewczyk,wyrzykow,kulaczyk,twieck@astrouw.edu.pl

⁵*Spitzer* Science Center, California Institute of Technology, Pasadena, CA 91125, USA; reach@ipac.caltech.edu

⁶Auckland Observatory, Auckland, New Zealand, gwchristie@christie.org.nz

⁷Michelson Science Center, California Institute of Technology, 770 South Wilson Ave., Pasadena, CA 91125, USA; bode@ipac.caltech.edu

⁸Department of Physics and Astronomy, Georgia State University, 29 Peachtree Center Avenue, Suite 400, Atlanta, GA 30303, USA.

⁹Department of Physics, Notre Dame University, Notre Dame, IN 46556, USA; bennett@nd.edu

¹⁰Center for Astrophysics, Cambridge, MA 02138, USA; fazio@cfa.harvard.edu

¹¹Department of Physics, University of California, San Diego, CA 92093, USA; griest@ucsd.edu

¹²Universidad de Concepción, Departamento de Física, Casilla 160-C, Concepción, Chile

¹³Institute of Astronomy Cambridge University, Madingley Rd., CB3 0HA Cambridge

¹⁴Princeton University Observatory, Princeton, NJ 08544, USA; bp@astro.princeton.edu

¹⁵The Observatories of the Carnegie Institute of Washington, 813 Santa Barbara Street, Pasadena, CA 91101, USA; gwp,ian@ociw.edu

velocity $\tilde{v} \sim 230 \text{ km s}^{-1}$, the typical value expected for halo lenses, but an order of magnitude smaller than would be expected for lenses lying in the Small Magellanic Cloud itself. The lens is a weak (i.e., non-caustic-crossing) binary, which complicates the analysis considerably but ultimately contributes additional constraints. Using a test proposed by Assef et al. (2006), which makes use only of kinematic information about different populations but does not make any assumptions about their respective mass functions, we find that the likelihood ratio is $\mathcal{L}_{\text{halo}}/\mathcal{L}_{\text{SMC}} = 20$. Hence, halo lenses are strongly favored but SMC lenses are not definitively ruled out. Similar *Spitzer* observations of additional lenses toward the Magellanic Clouds would clarify the nature of the lens population. The *Space Interferometry Mission* could make even more constraining measurements.

Subject headings: dark matter – galaxies: stellar content – gravitational lensing

1. Introduction

In a visionary paper written 40 years ago, Refsdal (1966) argued that two important but otherwise unmeasurable parameters of microlensing events could be determined by simultaneously observing the event from the Earth and a satellite in solar orbit. In modern language, these are the Einstein radius projected onto the observer plane, \tilde{r}_{E} , and the direction of lens-source relative proper motion. Since the Einstein timescale, t_{E} , is routinely measured for all events, these parameter determinations are equivalent to knowing the projected relative velocity, $\tilde{\boldsymbol{v}}$, whose magnitude is simply $\tilde{v} \equiv \tilde{r}_{\text{E}}/t_{\text{E}}$. Here, $\tilde{r}_{\text{E}} \equiv \text{AU}/\pi_{\text{E}}$, $t_{\text{E}} = \theta_{\text{E}}/\mu$,

$$\pi_{\text{E}} = \sqrt{\frac{\pi_{\text{rel}}}{\kappa M}}, \quad \theta_{\text{E}} = \sqrt{\kappa M \pi_{\text{rel}}}, \quad (1)$$

π_{E} is the microlens parallax, θ_{E} is the angular Einstein radius, π_{rel} and $\boldsymbol{\mu}$ are the lens-source relative parallax and proper motion, and $\kappa \equiv 4G/(c^2 \text{AU})$.

The practical importance of this suggestion became clear when the MACHO (Alcock et al. 1993) and EROS (Aubourg et al. 1993) collaborations reported the detection of microlensing events toward the Large Magellanic Cloud (LMC). In the course of time, MACHO (Alcock et al. 1997, 2000) have found about 15 such events and argued that these imply that about 20% of the Milky Way dark halo is composed of compact object (“MACHOs”), while EROS (Afonso et al. 2003; Tisserand et al. 2006) argued that their relative lack of such detections was consistent with all the events being due to stars in the Milky Way disk or the Magellanic Clouds (MCs) themselves. For any given individual event, it is generally impossible to tell (with only a measurement of t_{E}) where along the line of sight the lens lies,

and so one cannot distinguish among the three possibilities: Milky Way disk, Milky Way halo, or “self-lensing” in which the source and lens both lie in the same external galaxy.

However, as Bouteux & Gould (1996) argued, measurement of $\tilde{\mathbf{v}}$ might allow one to distinguish among these populations with good confidence: disk, halo, and MC lenses typically have \tilde{v} of 50 km s^{-1} , 300 km s^{-1} , and 2000 km s^{-1} , respectively. The high projected speed of MC lenses derives from the long “lever arm” that multiplies their small local transverse speed by the ratio of the distances from the observer and the lens to the source.

There are serious obstacles, both practical and theoretical to measuring $\tilde{\mathbf{v}}$. One obvious practical problem is simply launching a spacecraft with a suitable camera into solar orbit. But the theoretical difficulties also place significant constraints on the characteristics of that spacecraft. To understand these properly, one should think in terms of the “microlens parallax” $\boldsymbol{\pi}_E$, whose magnitude is $\pi_E \equiv \text{AU}/\tilde{r}_E$ and whose direction is the same as $\tilde{\mathbf{v}}$. Choosing a coordinate system whose x -axis is aligned with the Earth-satellite separation at the peak of the event, we can write $\boldsymbol{\pi}_E = (\pi_{E,\tau}, \pi_{E,\beta})$. Then to good approximation,

$$\boldsymbol{\pi}_E = (\pi_{E,\tau}, \pi_{E,\beta}) = \frac{\text{AU}}{d_\perp} \left(\frac{\Delta t_0}{t_E}, \Delta u_0 \right), \quad (2)$$

where d_\perp is the Earth-satellite separation (projected onto the plane of the sky), Δt_0 is the difference in time of event maximum as seen from the Earth and satellite, and Δu_0 is the difference in dimensionless impact parameter (determined from the maximum observed magnification).

Refsdal (1966) already realized that equation (2) implicitly contains a four-fold degeneracy: while $\Delta t_0/t_E$ is unambiguously determined, there are four different values of Δu_0 depending on whether the individual impact parameters are positive or negative (on one side of the lens or the other). See Figure 2 of Gould (1994). In fact, the situation is considerably worse than this. While t_0 is usually measured very precisely in individual microlensing events, u_0 typically has much larger errors because it is strongly correlated with three other parameters, the timescale, t_E , the source flux f_s , and the blended flux, f_b . For a satellite separated by $d_\perp \sim 0.2 \text{ AU}$, and a projected Einstein radius $\tilde{r}_E \sim 5 \text{ AU}$, errors in the impact-parameter determinations of only $\sigma(u_0) \sim 2\%$ would lead to fractional errors $\sigma(\pi_E)/\pi_E \sim \sqrt{2}\sigma(u_0)\tilde{r}_E/d_\perp \sim 70\%$. Happily, Gould (1995) showed that if the two cameras were essentially identical, so one knew a priori that the blended light was virtually identical for the Earth and satellite measurements, then the error in Δu_0 would be reduced far below the individual errors in u_0 , making the parallax determination once again feasible.

Unfortunately, this trick cannot be used on *Spitzer*, the first general purpose camera to be placed in solar orbit. The shortest wavelength at which *Spitzer* operates is L band

($3.6 \mu\text{m}$), implying that the camera’s sensitivity cannot be duplicated from the ground, both because of higher background and different throughput as a function of wavelength.

In principle, microlens parallaxes can also be measured from the ground. As with space-based parallaxes, one component of $\boldsymbol{\pi}_E$ can generally be measured much more precisely than the other. For most events, $t_E \ll \text{yr}$, and for these the Earth’s acceleration can be approximated as constant during the event. To the degree that this acceleration is aligned (anti-aligned) with the lens-source relative motion, it induces an asymmetry in the light curve, since the event proceeds faster (slower) before peak than afterward (Gould et al. 1994). This is characterized by the “asymmetry parameter” $\Gamma \equiv \boldsymbol{\pi}_E \cdot \boldsymbol{\alpha} = \pi_{E,\parallel} \alpha$, where $\boldsymbol{\alpha}$ is the apparent acceleration of the Sun projected onto the sky and normalized to an AU, and $\pi_{E,\parallel}$ is the component of $\boldsymbol{\pi}_E$ parallel to $\boldsymbol{\alpha}$. Since Γ is directly measurable from the light curve, one can directly obtain 1-D parallax information $\pi_{E,\parallel} = \Gamma/\alpha$ for these events, while the orthogonal component $\pi_{E,\perp}$ is measured extremely poorly (e.g., Ghosh et al. 2005; Jiang et al. 2005). While there are a few exceptions (Alcock et al. 2001a; Gould et al. 2004; Park et al. 2004), 2-D parallaxes can generally only be obtained for relatively long events $t_E \gtrsim 90$ days, and even for these, the $\boldsymbol{\pi}_E$ error ellipse is generally elongated in the $\pi_{E,\perp}$ direction (Poindexter et al. 2005).

Since *Spitzer* is in an Earth-trailing orbit and the SMC is close to the ecliptic pole, the $\pi_{E,\tau}$ direction (defined by the Earth-satellite separation vector) is very nearly orthogonal to the $\pi_{E,\parallel}$ direction (defined by the direction of the Sun). Recognizing this, Gould (1999) advocated combining the two essentially 1-D parallaxes from the Earth-*Spitzer* comparison and the accelerating Earth alone to produce a single 2-D measurement of $\boldsymbol{\pi}_E$. He noted that once the difficult problem of measuring $\pi_{E,\beta}$ was jettisoned, the satellite observations could be streamlined to a remarkable degree: essentially only 3 observations were needed, 2 at times placed symmetrically around the peak, which are sensitive to the offset in t_0 between the Earth and satellite, and a third at late times to set the flux scale. This streamlining is important from a practical point of view because target-of-opportunity (ToO) time on *Spitzer* incurs a large penalty. Gould (1999) noted that the components of $\boldsymbol{\pi}_E$ measured by the two techniques were not exactly orthogonal but argued (incorrectly as it turns out) that this had no significant consequences for the experiment. We return to this point below.

Here we analyze *Spitzer* and ground-based observations of the microlensing event OGLE-2005-SMC-001 to derive the first microlens parallax measurement using this technique.

2. Observations

OGLE-2005-SMC-001 ($\alpha_{J2000.0} = 0^{\text{h}}40^{\text{m}}28^{\text{s}}.5$, $\delta_{J2000.0} = -73^{\circ}44'46.1''$) was alerted by the OGLE-III Early Warning System (EWS, Udalski 2003) on 9 July 2005 (HJD' \equiv HJD-2450000 = 3561.37), approximately 23 days (and seven observations) into the 2005 OGLE-III observing season for the Small Magellanic Cloud (SMC). In fact, EWS issued an internal alert five days earlier, when there were only three 2005 points, but the OGLE team reacted cautiously because of the high rate of questionable alerts toward the SMC and because the source lies projected against a background galaxy, making it a potential supernova candidate. However, the event shows a modest, but unambiguous rise 140 days earlier, at the end of the 2004 season, which is inconsistent with a supernova, and the unmagnified source sits right in the middle of the red giant clump on the color-magnitude diagram (CMD), with $(V - I, I) = (0.92, 18.4)$. Moreover, the light curve is achromatic. These factors convinced us that this was genuine microlensing, leading us to exercise our *Spitzer* ToO option, which consisted of three 2-hour observations, two placed symmetrically around the peak and one at baseline. Once this decision was made, OGLE increased its density of coverage to 3–5 *I*-band observations per clear night. OGLE observations were obtained using the 1.3m Warsaw telescope at Las Campanas Observatory in Chile, operated by the Carnegie Institution of Washington. The photometry was reduced using standard OGLE-III data pipeline (Udalski 2003) based on the image subtraction technique, DIA (Woźniak 2000). Also many *V*-band observations were obtained during the event for monitoring achromaticity. There are *Spitzer* observations at four epochs (not three, as originally envisaged). These were centered at 2005 July 15 UT 20:02:40, 2005 Aug 25 UT 12:44:25, 2005 Sep 15 UT 20:13:53, and 2005 Nov 29 UT 10:24:40. The first, third, and fourth observations each lasted 2 hours and consisted of two sets of about 100 dithered exposures, each of 26.8 seconds. The second observation (in August) was 1 hour, consisting of one set of 99 dithered exposures, each of 26.8 seconds. It was obtained with director's discretionary time (DDT). All four were carried out simultaneously at 3.6 μm and 5.8 μm . However, the third observation (which took place at relatively high magnification) was supplemented by 30 minutes of very short exposures in all four IRAC filters to probe the detailed spectral energy distribution of the source. The reason for the additional DDT observation is discussed in detail in § 3.

As originally conceived, the experiment was to consist only of OGLE and *Spitzer* observations. However, unexpected complications led us to take additional data from other ground-based observatories as well as the *Hubble Space Telescope*.

Initially, we obtained some data using the 1.3 m SMARTS (former 2MASS) telescope at Cerro Tololo Interamerican Observatory (CTIO) in Chile simply as a precaution against possible future problems with the OGLE telescope. (In order to align different light curves,

it is generally necessary that they have some overlap, so one cannot wait for the problems to arise before beginning to take data.) However, as the event approached peak, we found that it could not be fit with a classical Paczyński (1986) model, even when augmented by parallax. We therefore began to intensively observe the event from both the OGLE and SMARTS telescopes in the hopes of obtaining enough data to determine the nature of the light curve anomaly. Similar considerations led us to begin observations using the 0.35m Nustrini telescope at the Auckland Observatory in New Zealand, which lies at a substantially different longitude and suffers from substantially different weather patterns than the two Chile telescopes.

Additionally, several high dispersion spectra were obtained at Las Campanas Observatory using 6.5m Magellan and 2.5m du Pont telescopes with echelle spectrographs at different magnifications in order to check for potential radial-velocity variations in the spectra of the magnified source.

Finally, the anomalous behavior made it prudent to get high-resolution images using *HST*, both to improve the modeling of blended light in the ground-based and *Spitzer* images, and to determine whether the apparent ground-based source could actually be resolved into multiple sources. We had *HST* ToO time to complement low-resolution space-based microlensing parallax observations, which was originally to be applied to observations by *Deep Impact*. With the probability low that these would be triggered as originally planned, we applied this time to obtain two orbits of observations of OGLE-2005-SMC-001. There were two epochs of (*V, I, J, H, K*) exposures, on 2005 Oct 1 and 2006 May 17/18, with exposure times of (300,200,351,351,639) seconds. The infrared observations were then repeated on 2006 Jun 25.

2.1. Error Rescaling

Errors from each ground-based observatory are rescaled to force χ^2 per degree of freedom close to unity. For the OGLE data, we find by inspecting the cumulative distribution of the normalized residuals $(\delta/\sigma)^2$, that the rescaling factor is not uniform over the data set. Here σ is the error reported by OGLE and δ is the deviation of the data from the model. We therefore rescale in 4 segments, which are separated at HJD = 2453100, 2453576, and 2453609, with rescaling factors 1.4, 1.9, 3.6, and 2.0. We tested two other error-rescaling schemes, one with no rescaling and the other with uniform rescaling of the OGLE data. We found that the solutions do not differ qualitatively when these alternate schemes are used.

2.2. *Spitzer* Data Reduction and Error Determination

Our scientific goals critically depend on obtaining high-precision IRAC photometry for each of the 4 epochs. See § 3.1. These 4 epochs are divided into 7 1-hour sub-epochs, each consisting of about 100 dithers, one sub-epoch for the second epoch and two for each of the other three epochs. Based on photon statistics alone, the best possible precision would be about 0.2% for the five sub-epochs near peak, and $\sim 0.4\%$ for the last two sub-epochs. However, there are three interrelated problems that must be overcome to even approach this potential. First, the images contain “stripes” produced by nearby bright stars, perhaps AGB stars, which (because the 3 near-peak observations took place over 60 days) appear at several different rotation angles. Indeed, we expended considerable effort repositioning each successive image to avoid having these stripes come too close to, or actually overlap, the microlensed target, but they inevitably did overlap some reference stars. Second, the microlensed source is blended with a neighboring star within $1''.3$, which is easily resolved in *HST* images and clearly resolved in OGLE images as well. Third, this problem is significantly complicated by the well-known fact that IRAC $3.6\ \mu\text{m}$ images are undersampled.

We apply the procedures of Reach et al. (2005) to perform aperture photometry on the Basic Calibrated Data (BCD), which includes array-location-dependent and “pixel-phase” photometric corrections at the few percent level. We choose 7 bright and isolated stars, which we select from the OGLE images. The *HST* frames are of course even better resolved, but they are too small to contain a big enough sample of reference stars. The centroid position of the target-star aperture on each of the (roughly 100) BCD dithers is determined by aligning the comparison stars to the OGLE coordinates. We determine the “internal error” for the target star and the comparison stars at each sub-epoch from the internal scatters in their measurements. This is typically very close to the photon limit. However, we find that the epoch-to-epoch scatter in the comparison stars is about 0.7%. While in principle this could be due to intrinsic variability, such variability is unlikely to be so pervasive at this level, particularly since any star showing variability in *I* band over several years was excluded as a reference star. Hence, we attribute this variation to unknown epoch-to-epoch systematics, and we assume that these affect the target in the same way that they affect the reference stars. Hence, we adopt 0.7% as our photometric error for each of the 7 *Spitzer* sub-epochs.

We also attempted to do point-spread-function (rather than aperture) photometry, making use of “Point Response Functions” available at the *Spitzer* Science Center website. However, we found that the reference stars showed greater scatter between sub-epochs with this approach and so adopted the results from aperture photometry.

3. Complications Alter Strategy and Analysis

Figure 1 shows the ground-based light curve with a fit to a standard (Paczynski 1986) model. The residuals are severe. The model does not include parallax. However, models that include parallax are quite similar. In the period before the peak, we were constantly refitting the light curve with every new night’s data in order to be able to predict the time of peak and so the time of the second ToO observation (which was supposed to be symmetric around the peak with the first). It became increasingly clear that the event was not standard microlensing, and we began to consider alternate possibilities, including binary source (also called “xallarap”), binary lens, and variable source. The last was especially alarming because if the variability were irregular, it would be almost impossible to model at the high precision required to carry out this experiment, particularly because the source might vary differently at I and L . Our concern about xallarap led us to obtain radial-velocity measurements at several epochs near the peak. These turned out to be the same within less than 1 km s^{-1} , which ruled out xallarap for all but the most pathologically face-on orbits. But regardless of the nature of the anomaly, it could potentially cause serious problems because much more and better data are required to accurately model complicated light curves than simple ones. Hence, as described in § 2, recognition of the anomaly caused us to significantly intensify our ground-based observations. Moreover, it also caused us to think more carefully about how we would extract parallax information from a more complicated light curve, and this led us to recognize a complication that affects even light curves that do not suffer from additional anomalies.

3.1. Need for Additional *Spitzer* Observation

Recall that $\pi_{E,\tau}$ is derived from the different peak time t_0 as seen from Earth and *Spitzer*: if the two *Spitzer* observations are timed so that the fluxes seen at Earth are equal to each other (one on the rising and one on the falling wing of the light curve), then the *Spitzer* fluxes will nevertheless be different, the first one being higher if the event peaks at *Spitzer* before the Earth. However, the two *Spitzer* fluxes may differ not only because *Spitzer* is displaced from the Earth along the direction of lens-source relative motion, but also if it is displaced in the orthogonal direction by *different amounts* at the two epochs. Gould (1999) recognized this possibility, but argued that the amplitude of this displacement could be determined from the measurement of $\pi_{E,\parallel}$, which is derived from the ground-based parallax measurement (i.e., from the asymmetry of the light curve). Hence, he argued that it would be possible to correct for this additional offset and still obtain a good measurement of $\pi_{E,\tau}$. Unfortunately, while it is true that the *amplitude* can be so derived, the *sign* of this correction is more difficult to

determine.

The problem can be understood by considering the work of Smith et al. (2003), who showed that ground-based microlensing parallaxes are subject to a two-fold degeneracy, essentially whether the source passes the lens on the same or opposite side of the Earth as the Sun. Within the geocentric formalism of Gould (2004), this amounts to switching the sign of the impact parameter u_0 (which by convention is normally positive) and leaving all other parameters essentially unchanged. Smith et al. (2003) derived this degeneracy under the assumption that the Earth accelerates uniformly during the course of the event. This is a reasonable approximation for short events, but is grossly incorrect for OGLE-2005-SMC-001, with its timescale of $t_E \sim 0.5$ yr. Nevertheless, this degeneracy can hold remarkably well even for relatively long events, particularly for $|u_0| \ll 1$. The sign of the correction to $\pi_{E,\tau}$ depends essentially on whether the *absolute value* of the impact parameter as seen from *Spitzer* is higher or lower than as seen from Earth. While the *algebraic* displacement of *Spitzer* along this direction can be predicted from the ground-based measurement of the parallax asymmetry (just as Gould 1999 argued), its effect on the absolute value of u_0 depends on whether u_0 is positive or negative.

If the parallax is sufficiently large, then the ground-based light curve alone can determine the sign of u_0 , and if it is sufficiently small, the difference between the two solutions is also very small and may not be significant. However, for intermediate values of the parallax, this degeneracy can be important. To understand how an additional *Spitzer* observation can help, consider an idealized set of four observations, one at peak, one at baseline, and two symmetrically timed around peak (as seen from Earth). Call these fluxes f_P , f_b , f_- , and f_+ . Consider now the ratio $[f_P - f_b]/[(f_- + f_+)/2 - f_b]$. If the impact parameter seen from *Spitzer* is higher than from Earth, this ratio will be lower for the *Spitzer* data than for the ground-based data. (Note that blended light, which may be different for the two sets of observations, cancels out of this expression.) In practice, we found from simulations that it was not necessary to have the three observations timed so perfectly. Hence, it was possible to plan both the additional DDT observation, as well as the second ToO observation to occur during regularly scheduled IRAC campaigns, so there was no 6.5 hour penalty for either observation. Hence, the net cost to *Spitzer* time was less than would have been the case for a single precisely timed ToO observation.

In brief, the above considerations demonstrate that the Gould (1999) technique requires a total of four observations, not three as originally proposed. Moreover, these observations do not have to be so precisely timed as Gould (1999) originally imagined. See Figure 2 for a visual explanation of these arguments.

3.2. Eight-Fold Way

Ultimately, we found that the anomaly was caused by a binary lens. Binary lenses are subject to their own discrete degeneracies. This means that analysis of the event is impacted by two distinct classes of discrete degeneracies, those due to parallax and to binarity. The discrete parallax degeneracy, as summarized in § 3.1, takes the impact parameter $u_0 \rightarrow -u_0$ and (because $u_0 \ll 1$) leaves other parameters changed by very little (see Gould 2004).

The discrete binary degeneracy is between wide and close binaries. Here “wide” means $b \gg 1$ and “close” means $b \ll 1$, where b is the angular separation between the two binary components in units of θ_E , (for which we give and justify our convention in § 4.1). It sends $(b_c, q_c) \rightarrow (b_w, q_w)$,

$$b_w = \frac{1 + q_c}{1 - q_c} b_c^{-1}, \quad q_w = \frac{q_c}{(1 - q_c)^2} \quad (3)$$

and leaves other parameters roughly unchanged. Here q is the mass ratio of the lens, with the convention that for q_w , the component closer to the source trajectory goes in the denominator of the ratio. In both cases, the central magnification pattern is dominated by a 4-cusp caustic.

This degeneracy was first discovered empirically by Albrow et al. (1999) and theoretically by Dominik (1999) and can be incredibly severe despite the fact that the two caustics are far from identical: the solutions can remain indistinguishable even when there are two well-observed caustic crossings (An 2005).

In the present case, the deviations from a simple lens are not caused by caustic crossings, but rather by a close approach to a cusp, which makes this degeneracy even more severe. In fact, the caustic is symmetric enough that the approach may almost equally well be to either of two adjacent cusps. That is, the cusp degeneracy would be “perfect” if the cusp were four-fold symmetric, and it is only the deviation from this symmetry that leads to distinct solutions for different cusp approaches.

In brief, the lens geometry is subject to an 8-fold discrete degeneracy, 2-fold for parallax, 2-fold for wide/close binary, and 2-fold for different cusp approaches.

4. Binary Orbital Motion

Of course all binaries are in Kepler orbits, but it is usually possible to ignore this motion in binary-lens analyses. Stated less positively, it is rarely possible to constrain any binary orbital parameters from microlensing light curves. In the few known exceptions, (Albrow et al. 2000; An et al. 2002), the light curve contained several well-measured caustic crossings

that pinned down key times in the trajectory to $O(10^{-5})$ of an Einstein crossing time. Hence, we did not expect to measure binary rotation in the present case in which there are no such crossings.

We were nevertheless led to investigate rotation by the following circumstance. When we initially analyzed the event using only ground-based data, we found that the best fit (for all 8 discrete solutions) had negative blended light, roughly -10% of the source light, but with large errors and so consistent with zero at the 1.5σ level. This was not unexpected. As mentioned in § 1, the component of the microlens parallax perpendicular to the Sun, $\pi_{E,\perp}$, is generally poorly constrained by ground-based data alone. The reason for this is that small changes in $\pi_{E,\perp}$, the Einstein timescale t_E , the impact parameter u_0 , the source flux f_s , and the blended flux, f_b , all induce distortions in the light curve that are symmetric about the peak, and hence all these parameters are correlated. Thus, the large errors (and consequent possible negative values) of f_b are just the obverse of the large errors in $\pi_{E,\perp}$. Indeed, this is the reason for adding in *Spitzer* observations.

We found, however, when the *Spitzer* observations were added, that while the blending errors were indeed reduced, the actual value of the blending remained highly negative, near -10% . This prompted us to look for other physical effects that could induce distortions in the light curve that might masquerade as negative blending. First among these was binary orbital motion. Before discussing this motion, we first review microlensing by static binaries.

4.1. Static Binary Lens Parameters

Point-lens microlensing is described by three geometric parameters, the impact parameter u_0 (smallest lens-source angular separation in units of θ_E), the time at which the separation reaches this minimum t_0 , and the Einstein crossing time $t_E = \theta_E/\mu$, where μ is the lens-source relative proper motion.

In binary lensing, there are three additional parameters, the projected separation of the components (in units of θ_E) b , the mass ratio of the components q , and the angle of the source-lens trajectory relative to the binary axis, ϕ . Moreover the first three parameters now require more precise definition because there is no longer a natural center to the system. One must therefore specify where the center of the system is. Then u_0 becomes the closest approach to this center and t_0 the time of this closest approach. Finally, t_E is usually taken to be the time required to cross the Einstein radius defined by the *combined* mass of the two components.

In fact, while computer programs generally adopt some fairly arbitrary point (such

as the midpoint between the binaries or the binary center of mass), the symmetries of individual events can make other choices much more convenient. That is certainly the case here. Moreover, symmetry considerations that are outlined below will also lead us to adopt a somewhat non-standard t_E for the wide-binary case, namely the timescale associated with the mass that is closer to the source trajectory, rather than the total mass. To be consistent with this choice, we also express b as the separation between wide components in units of the Einstein radius associated with the nearest mass (rather than the total mass).

As is clear from Figure 1, the light curve is only a slightly perturbed version of standard (point-lens) microlensing, which means that it is either generated by the source passing just outside the central caustic of a close binary (that surrounds both components) or just outside one of the two caustics of a wide binary (each associated with one component). In either case, the standard point-lens parameters u_0 and t_0 will be most closely reproduced if the lens center is placed at the so-called “center of magnification”. For close binaries this lies at the binary center of mass. For wide binaries, it lies $q(1+q)^{-1/2}b^{-1}$ from the component that is closer to the trajectory. Hence, it is separated by very nearly $bq/(1+q)$ from the center of mass. This will be important in deriving equation (4), below.

For light curves passing close to the diamond caustic of a close binary, the standard Einstein timescale (corresponding to the total mass) will be very close to the timescale derived from the best-fit point lens of the same total mass. However, for wide binaries, the standard Einstein timescale is longer by a factor $(1+q)^{1/2}$, where q is the ratio of companion (whether heavier or lighter) to the component that is approached most closely. This is because the magnification is basically due just to this latter component (with the companion contributing only minor deviations via its shear), while the usual Einstein radius is based on the *total* mass. For wide binaries, we therefore adopt an Einstein radius and Einstein timescale reduced by this same factor.

The advantage of adopting these parameter definitions is that, being fairly well fixed by the empirical light curve, they are only weakly correlated with various other parameters, some of which are relatively poorly determined.

4.2. Binary Orbital Parameters

While close and wide binaries can be (and in the present case are) almost perfectly degenerate in the static case, binary orbital motion has a radically different effect on their respective light curves. Note first that while 7 parameters would be required to fully describe the binary orbital motion, even in the best of cases it has not proven possible to constrain

more than 4 of them (Albrow et al. 2000; An et al. 2002). Two of these have already been mentioned, i.e., b and q , from the static case. For the two binaries for which additional parameters have been measured, these have been taken to be a uniform rotation rate ω and a uniform binary-expansion rate \dot{b} .

This choice is appropriate for close binaries because for these, the center of mass is the same as the center of magnification. Hence the primary effects of binary motion are rotation of the magnification pattern around the center of magnification and change of the magnification pattern due to changing separation. Both of these changes may be (probably are) nonuniform, but as the light curves are insensitive to such subtleties, the simplest approximation is uniform motion.

However, the situation is substantially more complicated for wide binaries, consideration of which leads to a different parameterization. Recall that the wide-binary center of magnification is not at the center of mass, and indeed is close to one of the components. Hence, as the binary rotates, the center of magnification rotates basically with that component. Nominally, the biggest effect of this rotation is the resulting roughly linear motion of the lens center of magnification relative to the source. However, the linear component of this motion, i.e., the first derivative of the motion at the peak of the event, is *already* subsumed in the source-lens relative motion in the static-binary fit. The first new piece of information about the binary orbital motion is the second derivative of this motion, i.e., the acceleration. Note that the direction of this acceleration is known: it is along the binary axis. Moreover, for wide binaries, Kepler’s Third Law predicts that the periods will typically be much longer than the Einstein timescale, so to a reasonable approximation, this direction remains constant during the event. We designate the acceleration (in Einstein radii per unit time squared) as α_b .

The parameter α_b is related to the distance to the lens in a relatively straightforward way. For simplicity, assume for the moment that the center of magnification is right at the position of the component that is closer to the source trajectory (instead of just near it). The 3-dimensional acceleration of the component is $a = GM_2/(br_E \csc i)^2$, where M_2 is the mass of the companion to the closer component, r_E is the physical Einstein radius, and i is the angle between the binary axis and the line of sight. Hence, $\alpha_b = a \sin i/r_E = (q/b^2)GM_1 \sin^3 i/r_E^3$, where M_1 is the mass of the closer component. This can be simplified with the aid of the following three identities: 1) $4GM_1/c^2 = \tilde{r}_E \theta_E$, 2) $r_E = D_L \theta_E$, 3) $r_E/\tilde{r}_E = D_{LS}/D_S$. Here D_L and D_S are the distances to the lens and source, and $D_{LS} = D_S - D_L$. We then find,

$$\frac{\alpha_b}{\pi_E} = \frac{\gamma c^2 \sin^3 i}{4D_L \text{AU}} \frac{D_S^2}{D_{LS}^2}, \quad (4)$$

where $\gamma \equiv q/b^2$ is the shear. Note that the shear determines the size of the caustic and so is

one of the parameters that is most robustly determined from the light curve. If we were to take account of the offset between M_1 and the center of magnification, the r.h.s. of equation (4) would change fractionally by of order b^{-2} .

4.3. Summary of Parameters

Thus, the model requires a total of 10 geometrical parameters in addition to the 8 flux parameters (f_s and f_b for each of the 3 ground-based observatories plus *Spitzer*). These are the three standard microlensing parameters, t_0, u_0, t_E (the time of closest approach, separation at closest approach in units of θ_E , and Einstein timescale), the three additional static-binary parameters b, q, ϕ (the binary separation in units of θ_E , the binary mass ratio, and the angle of the source trajectory relative to the binary axis), the two binary-orbit parameters, \dot{b} and either ω (close) or α_b (wide), and the two parallax parameters, $\boldsymbol{\pi}_E = (\pi_{E,N}, \pi_{E,E})$, where N and E represent the North and East directions. These must be specified for 8 different classes of solutions.

5. Search for Solutions

We combine two techniques to identify all viable models of the observed microlensing light curve: stepping through parameter space on a grid (grid-search) and Markov Chain Monte Carlo (MCMC) (Doran & Mueller 2003).

We begin with the simplest class of binary models, i.e., without parallax or rotation. Hence, there are six geometric parameters, $t_0, u_0, t_E, b, q,$ and ϕ . We consider classes of models with (b, q, ϕ) held fixed, and vary (t_0, u_0, t_E) to minimize χ^2 . (Note that for each trial model, f_s and f_b can be determined algebraically from a linear fit, so their evaluations are trivial.) This approach identifies four solutions, i.e. $(2 \text{ cusp-approaches}) \times (\text{wide/close degeneracy})$. We then introduce parallax, and so step over models with $(b, q, \phi, \pi_{E,N}, \pi_{E,E})$ held fixed, working in the neighborhood of the (b, q, ϕ) minima found previously. The introduction of parallax brings with it the $\pm u_0$ degeneracy, and so there are now 8 classes of solutions.

Next we introduce rotation. We begin by employing grid search and find, somewhat surprisingly, that several of the eight (close/wide, $\pm u_0$, on/off-axis cusp) classes of solutions have more than one minimum in (ω, \dot{b}) for close binaries or (α_b, \dot{b}) for wide binaries. We then use each of these solutions as seeds for MCMC and find several additional minima that were too close to other minima to show up in the grid search. Altogether there are 20 separate

minima, 12 for close binaries and 8 for wide binaries.

We use MCMC to localize our solutions accurate to about 1σ and to determine the covariance matrix of the parameters. In MCMC, one moves randomly from one point in parameter space to another. If the χ^2 is lower, the new point is added to the “chain”. If not, one draws a random number and adds the new point only if this number is lower than relative probability ($\exp(-\Delta\chi^2/2)$). If the parameters are highly correlated (as they are in microlensing) and the random trial points are chosen without reference (or without proper reference) to these covariances, then the overwhelming majority of trial points are rejected. We therefore sample parameter space based on the covariance matrix drawn from the previous “links” in the chain. During the initial “burning in” stage of the MCMC, we frequently evaluate the covariance matrix (every 100 “links”) until it stabilizes. Then we hold the covariance matrix fixed in the simulation (Doran & Mueller 2003). From the standpoint of finding the best χ^2 , one can combine linear fits for the flux parameters f_s and f_b with MCMC for the remaining parameters. However, since part of our MCMC objective is to find the covariances, we treat $(f_s, f_b)_{\text{OGLE}}$ as MCMC parameters while fitting for the remaining four flux parameters analytically.

In order to reduce the correlations among search parameters, we introduce the following parameter combinations into the search: $t_{\text{eff}} \equiv u_0 t_E$, $f_{\text{base}} = f_s + f_b$, $f_{\text{max}} \equiv f_s/u_0$, and $\gamma \equiv q/b^2$ (wide) or $Q \equiv b^2 q/(1+q)^2$ (close). Because these are directly related to features in the light curve, they are less prone to variation than the naive model parameters. The effective timescale t_{eff} is $1/\sqrt{12}$ of the full-width at half-maximum, f_{base} is just the flux at baseline, and f_{max} is the flux at maximum. The scale of the Chang-RRefsdal (1979, 1984) distortion (which governs the binary perturbation) is given by the shear γ for wide binaries and by the quadrupole Q for close binaries.

The MCMC “chain” automatically samples points in the neighborhood of the minimum with probability density proportional to their likelihoods, $\exp(-\chi^2/2)$. Somewhat paradoxically, this means that for higher-dimensional problems, it does not actually get very close to the minimum. Specifically, for a chain of length N sampling an m -dimensional space, there will be only one point for which $\Delta\chi^2$ (relative to the minimum) obeys $\Delta\chi^2 < Y$, where $P[\chi^2(m \text{ dof}) < Y] = N^{-1}$. Hence, for $m \gg 1$ one requires a chain of length $N \sim e^{1/2}(m/2)!2^{m/2}$ to reach 1σ above the true minimum, or $N \sim 10^{4.9}$ for $m = 12$. Further improvements scale only as $\sim N^{1/m}$. Hence, to find the true minimum, we construct chains in which the rejection criterion is calculated based on $\exp(-25\chi^2/2)$ rather than $\exp(-\chi^2/2)$. However, when calculating error bars and covariances, or when integrating over the MCMC, we use the $\exp(-\chi^2/2)$ chain.

5.1. Convergence

A general problem in MCMC fitting is to determine how well the solution “converges”, that is, how precisely the “best fit” solution is reproduced when the initial seed solution is changed. In our case, the problem is the opposite: MCMC clearly does not converge to a single minimum, and the challenge is to find all the local minima. We described our procedure for meeting this challenge above, first by identifying 8 distinct regions of parameter space semi-analytically, and then exploring these with different MCMC seeds. This procedure led to well-defined minima (albeit a plethora of them), whose individual structures were examined by putting boundaries into the MCMC code that prevented the chain from “drifting” into other minima. We halted our subdivision of parameter space when the structure on the χ^2 surface fell to of order $\Delta\chi^2 \sim 1$, regarding the $\Delta\chi^2 \lesssim 1$ region as the zone of convergence. As mentioned above, we located the final minimum by artificially decreasing the errors by a factor of 5, again making certain that the resulting (exaggerated) χ^2 surface was well behaved.

6. Solution Triage

Table 1 gives parameter values and errors for a total of 20 different discrete solutions, which are labeled by (C/W) for close/wide binary, (+/–) for the sign of u_0 , (||/⊥) for solutions that are approximately parallel or perpendicular to the binary axis, and then by alphabetical sequential for different viable combinations of rotation parameters. In Table 1, we allow a free fit to blending.

Note that some solutions have severe negative blending. While it is possible in principle that these are due to systematic errors, the fact that other solutions have near-zero blending and low χ^2 implies that the negative-blending solutions probably have lens geometries that do not correspond to the actual lens. Other solutions have relatively high χ^2 and so are also unlikely. Solutions with χ^2 that is less than 9 above the minimum have their χ^2 displayed in boldface, while the remaining solutions are shown in normal type.

There are several reasons to believe that the blending is close to zero. First, the source appears isolated on our K -band NICMOS *HST* images, implying that if it is blended, this blended light must be within of order 100 mas of the source. As the density of sources in the *HST* images is low, this is a priori very unlikely unless the blended light comes from a companion to the source or the lens. Moreover, all the near neighbors of the source on the *HST* image are separately resolved by the OGLE photometry, so if there is blended light in the OGLE photometry then it must also be blended in the *HST* images. Second, the

$V - I$ color of the source, which can be derived by a model-independent regression of V flux on I flux, is identical within measurement error to the color of the baseline light from the combined source and (possible) blend. This implies that either 1) the source is unblended, 2) it is blended by another star of nearly the same color as the source, or 3) it is blended by a star that is so faint that it hardly contributes to the color of the blend. The second possibility is strongly circumscribed by the following argument. The source is a clump star. On the SMC CMD, there are first ascent giants of color similar to the source from the clump itself down to the subgiant branch about 2.5 mag below the clump. Thus, in principle, the blended light could lie in the range $0.1 \lesssim f_b/f_s \lesssim 1$ without causing the baseline color to deviate from the source color. However, there are no solutions in Table 1 with blending this high. There is one low- χ^2 solution with $f_b/f_s \sim 0.06$, but this would be 3 mag below the clump and so below the subgiant branch. If we restrict the blend to turnoff colors, i.e., $V - I = 0.6$, then the color constraint implies $f_b/f_s = 0.01 \pm 0.01$, which is negligibly small from our perspective. Thus, while it is possible in principle that the source is blended with a reddish subgiant, the low stellar density in the *HST* image, the low frequency of such subgiants on the CMD, and the difficulty of matching color constraints even with such a star, combine to make this a very unlikely possibility. We therefore conduct the primary analysis assuming zero blending, as listed in Table 2. Again, the $\Delta\chi^2 < 9$ solutions are marked in boldface. Note that most solutions in Table 1 are reasonably consistent with zero blending, which is the expected behavior for the true solution provided it is not corrupted by systematic errors. For these, the χ^2 changes only modestly from Table 1 to Table 2. However, several solutions simply disappear from Table 2. This is because, in some cases, forcing the blending to zero has the effect of merging two previously distinct binary-rotation minima.

The main parameters of interests are $\boldsymbol{\pi}_E$ and the closely related quantity $\tilde{\mathbf{v}}$. However, for reasons that will be explained below, $\tilde{\mathbf{v}}$ can be reliably calculated only for the close solutions, but not the wide solutions. Hence, we focus first on $\boldsymbol{\pi}_E$.

Figure 3 shows error ellipses for all solutions, color-coded by according to $\Delta\chi^2$ relative to the global minimum. The right-hand panels show the solutions presented in Tables 1 and 2, which include the *Spitzer* data. The left-hand panels exclude these data. The upper panels are based on a free fit for blending whereas the lower panels are constrained to zero blending for the OGLE dataset. Comparing the two upper panels, it is clear that when blending is a fitted parameter, the *Spitzer* data reduce the errors in the $\pi_{E,\perp}$ direction by about a factor of 3. However, once the blending is fixed (lower panels), the *Spitzer* data have only a modest additional effect. This is expected since $\pi_{E,\perp}$ is correlated with blending and one can simultaneously constrain both parameters either by constraining $\pi_{E,\perp}$ with *Spitzer* data or just by fixing the blending by hand. Figure 4 shows the best overall zero-blending fit to the data.

6.1. Wide-Binary Solutions

All eight wide solutions are effectively excluded. When a free fit to blending is allowed, their χ^2 's are already significantly above the minimum. When zero blending is imposed, only five independent solutions survive and those that have negative blending are driven still higher. In all five cases to $\Delta\chi^2 > 16$.

6.2. Close-Binary Solutions

Eight Of the 11 close solutions survive the imposition of zero blending. Of these, only one has $\Delta\chi^2 < 4$, and only another two have $\Delta\chi^2 < 8.7$ relative to the best zero-blending solution. We focus primarily on these three, which all have best-fit parallaxes in the range $0.030 < \pi_E < 0.047$ and projected velocities in the range $210 \text{ km s}^{-1} < \tilde{v} < 330 \text{ km s}^{-1}$. These projected velocities are of the order expected for halo lenses but are about 1 order of magnitude smaller than those expected for SMC self lensing. Note that because there are multiple solutions, the errors in \tilde{v} are highly non-Gaussian and are best judged directly from Figures 5 and 6 (below) rather than quoting a formal error bar.

7. Lens Location

When Alcock et al. (1995) made the first measurement of microlensing parallax, they developed a purely kinematic method of estimating the lens distance (and so mass) based on comparison of the measured value of \tilde{v} with the expected kinematic properties of the underlying lens population. Starting from this same approach, Assef et al. (2006) devised a test that uses the microlens parallax measurement to assign relative probabilities to different lens populations (e.g., SMC, Galactic halo, Galactic disk) based solely on the *kinematic* characteristics of these populations, and without making prior assumptions about either the mass function or the density normalization of any population. This is especially useful because, while a plausible guess can be given for the mass function and normalization of SMC lenses, nothing is securely known about a putative Galactic halo population. In the present case, the high projected velocity \tilde{v} immediately rules out Galactic-disk lenses, so we restrict consideration to the other two possibilities.

We begin by recapitulating the Assef et al. (2006) test in somewhat more general form. The differential rate of microlensing events of fixed mass M (per steradian) is

$$d^{(6)}\Gamma(M) \equiv \frac{d^6\Gamma(M)}{d^2v_L d^2v_S dD_L dD_S} = f_L(\mathbf{v}_L) f_S(\mathbf{v}_S) D_S^2 \nu_S(D_S) \nu_L(D_L) 2\tilde{v} \tilde{r}_E \frac{D_{LS}^2}{D_S^2}, \quad (5)$$

where $f_L(\mathbf{v}_L)$ and $f_S(\mathbf{v}_S)$ are the two-dimensional normalized velocity distributions of the lenses and sources, ν_L and ν_S are the density distributions of the lenses and sources, \tilde{v} is an implicit function of $(D_L, D_S, \mathbf{v}_L, \mathbf{v}_S)$, and \tilde{r}_E is an implicit function of (D_L, D_S, M) . The method is simply to evaluate the likelihood

$$\mathcal{L} = \frac{\int d^2v_L d^2v_S dD_L dD_S d^{(6)}\Gamma(M) \exp[-\Delta\chi^2(\tilde{\mathbf{v}})/2]}{\int d^2v_L d^2v_S dD_L dD_S d^{(6)}\Gamma(M)} \quad (6)$$

for each population separately, and then take the ratio of likelihoods for the two populations: $\mathcal{L}_{\text{ratio}} \equiv \mathcal{L}_{\text{halo}}/\mathcal{L}_{\text{SMC}}$. Here, $\Delta\chi^2(\tilde{\mathbf{v}})$ is the difference of χ^2 relative to the global minimum that is derived from the microlensing light curve. Note that all dependence on M disappears from \mathcal{L} . Equation (6) can be simplified in different ways for each population. In both cases, we express the result in terms of $\mathbf{\Lambda}$,

$$\mathbf{\Lambda} \equiv \frac{\tilde{\mathbf{v}}}{\tilde{v}^2} = \frac{\boldsymbol{\pi}_E t_E}{\text{AU}}, \quad (7)$$

rather than $\tilde{\mathbf{v}}$, because it is better behaved in the neighborhood of $\mathbf{\Lambda} = 0$, just as trigonometric parallax is better behaved near zero than its inverse, distance.

7.1. Halo Lenses

For halo lenses, the depth of the SMC is small compared to D_{LS} and the internal dispersion of SMC sources is small compared to the bulk motion of the SMC. Hence, one can essentially drop the three integrations over SMC sources, implying

$$\tilde{\mathbf{v}} = \frac{D_S}{D_{\text{LS}}}\mathbf{v}_L - \mathbf{v}_{\oplus} - \frac{D_L}{D_{\text{LS}}}\mathbf{v}_{\text{SMC}}, \quad (8)$$

where \mathbf{v}_L , \mathbf{v}_{\oplus} , and \mathbf{v}_{SMC} are the velocities of the lens, the “geocentric frame”, and the SMC (all in the Galactic frame) projected on the plane of the sky. The “geocentric frame” is the frame of the Earth at the time of the peak of the event. It is the most convenient frame for analyzing microlensing parallax (Gould 2004) and for this event is offset from the heliocentric frame by

$$(v_{\odot, \text{N}}, v_{\odot, \text{E}}) - (v_{\oplus, \text{N}}, v_{\oplus, \text{E}}) = (-24.9, -15.5) \text{ km s}^{-1}. \quad (9)$$

We assume an isotropic Gaussian velocity dispersion for the lenses with $\sigma_{\text{halo}} = v_{\text{rot}}/\sqrt{2}$, where $v_{\text{rot}} = 220 \text{ km s}^{-1}$. After some manipulations (and dropping constants that would cancel out between the numerator and denominator) we obtain

$$\mathcal{L}_{\text{halo}} = \frac{\int \exp[-\Delta\chi^2(\mathbf{\Lambda})/2] g_{\text{halo}}(\mathbf{\Lambda}, D_L) dD_L d\Lambda_{\text{North}} d\Lambda_{\text{East}}}{\int g_{\text{halo}}(\mathbf{\Lambda}, D_L) dD_L d\Lambda_{\text{North}} d\Lambda_{\text{East}}}, \quad (10)$$

where

$$g_{\text{halo}}(\mathbf{\Lambda}, D_L) = \exp(-v_L^2/2\sigma_{\text{halo}}^2)\nu_{\text{halo}}(D_L)\Lambda^{-5}D_{\text{LS}}^{7/2}D_L^{1/2}, \quad (11)$$

and where v_L is an implicit function of $\mathbf{\Lambda}$ through equations (7) and (8). We adopt $\nu_{\text{halo}}(\mathbf{r}) = \text{const}/(a_{\text{halo}}^2 + r^2)$, where $a_{\text{halo}} = 5$ kpc and the Galactocentric distance is $R_0 = 7.6$ kpc. We adopt $\mathbf{v}_{\odot} = (10.1, 224, 6.7)$ km s⁻¹ in Galactic coordinates, which leads to a 2-dimensional projected velocity of $(v_{\odot, \text{N}}, v_{\odot, \text{E}}) = (126, -126)$ km s⁻¹ toward the SMC source. From our assumed distances $D_{\text{SMC}} = 60$ kpc and the SMC's measured proper motion of $(-1.17 \pm 0.18, +1.16 \pm 0.18)$ (Kallivayalil et al. 2006), we obtain,

$$(v_{\text{SMC}, \text{N}}, v_{\text{SMC}, \text{E}}) - (v_{\odot, \text{N}}, v_{\odot, \text{E}}) = (-333, 330) \text{ km s}^{-1}. \quad (12)$$

7.2. SMC Lenses

For the SMC, we begin by writing

$$\tilde{\mathbf{v}} = \frac{\mathbf{v}_L/D_L - \mathbf{v}_S/D_S}{D_L^{-1} - D_S^{-1}} = \mathbf{v}_S + \frac{D_S}{D_{\text{LS}}} \Delta \mathbf{v} \rightarrow \mathbf{v}_{\text{SMC}} - \mathbf{v}_{\oplus} + \frac{D_{\text{SMC}}}{D_{\text{LS}}} \Delta \mathbf{v}, \quad (13)$$

where \mathbf{v}_L and \mathbf{v}_S are now measured in the geocentric frame and $\Delta \mathbf{v} \equiv \mathbf{v}_L - \mathbf{v}_S$. The last step in equation (13) is an appropriate approximation because the SMC velocity dispersion is small compared to its bulk velocity and $D_{\text{LS}} \ll D_S$.

We now assume that the sources and lenses are drawn from the same population, which implies that the dispersion of $\Delta \mathbf{v}$ is larger than those of \mathbf{v}_L and \mathbf{v}_S by $2^{1/2}$. We assume that this is isotropic with Gaussian dispersion σ_{SMC} . Again making the approximation $D_S \rightarrow D_{\text{SMC}}$, we can factor the integrals in equation (6) by evaluating the density integral

$$\eta(D_{\text{LS}}) = \int dD_L \nu(D_L) \nu(D_L + D_{\text{LS}}), \quad (14)$$

where $\nu = \nu_L = \nu_S$. We then obtain

$$\mathcal{L}_{\text{SMC}} = \frac{\int \exp[-\Delta\chi^2(\mathbf{\Lambda})/2] g_{\text{SMC}}(\mathbf{\Lambda}, D_{\text{LS}}) dD_{\text{LS}} d\Lambda_{\text{North}} d\Lambda_{\text{East}}}{\int g_{\text{SMC}}(\mathbf{\Lambda}, D_{\text{LS}}) dD_{\text{LS}} d\Lambda_{\text{North}} d\Lambda_{\text{East}}}, \quad (15)$$

where

$$g_{\text{SMC}}(\mathbf{\Lambda}, D_L) = \exp[-(\Delta v)^2/4\sigma_{\text{SMC}}^2] \eta(D_{\text{LS}}) D_{\text{LS}}^{7/2} \Lambda^{-5}, \quad (16)$$

and where Δv is an implicit function of $\mathbf{\Lambda}$ through equations (7) and (13).

7.3. SMC Structure

In order to evaluate equation (16) one must estimate σ_{SMC} as well as the SMC density ν along the line of sight, which is required to compute $\eta(D_{\text{LS}})$. This requires an investigation of the structure of the SMC.

In sharp contrast to its classic “Magellanic irregular” appearance in blue light, the SMC is essentially a dwarf elliptical galaxy whose old population is quite regular in both its density (Zaritsky et al. 2000) and velocity (Harris & Zaritsky 2006) distributions. Harris & Zaritsky (2006) find that after removing an overall gradient (more below), the observed radial velocity distribution is well fit by a Gaussian with $\sigma = 27.5 \text{ km s}^{-1}$, which does not vary significantly over their $4^\circ \times 2^\circ$ (RA,Dec) field.

We adopt the following SMC parameters for the 1-dimensional dispersion σ_{SMC} , the tidal radius r_t , and the density profile (along the line of sight), $\nu(r) = \text{const}/(a_{\text{SMC}}^2 + r^2)^{n/2}$,

$$\sigma_{\text{SMC}} = 25.5 \text{ km s}^{-1}, \quad r_t = 6.8 \text{ kpc}, \quad a_{\text{SMC}} = 1 \text{ kpc}, \quad n = 3.3, \quad (17)$$

as we now justify.

The $\sigma = 27.5 \text{ km s}^{-1}$ dispersion reported by Harris & Zaritsky (2006) includes measurement errors. When the reported errors (typically 10 km s^{-1} per star) are included in the fit, this is reduced to $\sigma_{\text{SMC}} = 24.5 \text{ km s}^{-1}$. However, these reported errors may well be too generous: the statistical errors (provided by D. Zaritsky 2006) are typically only $2\text{--}3 \text{ km s}^{-1}$, the reported errors being augmented to account for systematic errors. If the statistical errors are used, we find $\sigma_{\text{SMC}} = 26.5 \text{ km s}^{-1}$. D. Zaritsky (2006, private communication) advocates an intermediate value for this purpose, which leads to $\sigma_{\text{SMC}} = 25.5 \text{ km s}^{-1}$.

The old stellar population in the SMC is rotating at most very slowly. Harris & Zaritsky (2006) report a gradient across the SMC of $8.3 \text{ km s}^{-1} \text{ deg}^{-1}$, which they note is a combination of the traverse velocity of the SMC and the solid-body component of internal bulk motion. As the SMC proper motion was poorly determined at the time, Harris & Zaritsky (2006) did not attempt to disentangle these two. However, Kallivayalil et al. (2006) have now measured the SMC proper motion to be $(\mu_{\text{N}}, \mu_{\text{E}}) = (-1.16 \pm 0.18, 1.17 \pm 0.18) \text{ mas yr}^{-1}$. We refit the Harris & Zaritsky (2006) data and find $\nabla v_r = (-10.5 \pm 1.4, 5.0 \pm 0.7) \text{ km s}^{-1} \text{ deg}^{-1}$. Subtracting these two measurements (including errors and covariances) we obtain a net internal rotation of $5.2 \pm 1.6 \text{ km s}^{-1} \text{ deg}^{-1}$ with a position angle of $183^\circ \pm 30^\circ$. Since this rotation is due north-south (within errors), a direction for which the data have a baseline of only $\sim \pm 1^\circ$, and since solid-body rotation is unlikely to extend much beyond the core, it appears that the amplitude of rotational motion is only about 5 km s^{-1} , which is very small compared to the dispersion, σ_{SMC} . Hence, we ignore it. In addition, we note that this rotation is misaligned

with the HI rotation axis (Stanimirović et al. 2004) by about 120° , so its modest statistical significance may indicate that it is not real.

As we will describe below, our likelihood estimates are fairly sensitive to the tidal radius r_t of the SMC. Proper determination of the tidal radius is a complex problem. Early studies, made before dark matter was commonly accepted, were carried out for Kepler potentials and in analogy with stellar and solar-system problems (e.g. King 1962). Read et al. (2006) have calculated tidal radii for a range of potentials and also for an orbital parameter α that ranges from -1 for retrograde to $+1$ for prograde. We choose $\alpha = 0$ as representative and evaluate their expression for an isothermal potential and for the satellite being close to pericenter (as is appropriate for the SMC):

$$\frac{r_t}{D} = \frac{\sigma_{\text{sat}}}{\sigma_{\text{host}}} \left(1 + \frac{2 \ln \xi}{1 - \xi^{-2}} \right)^{-1/2}. \quad (18)$$

Here, ξ is the ratio of the apocenter to the pericenter of the satellite orbit, D is the pericenter distance, and σ_{sat} and σ_{host} are the respective *halo* velocity dispersions. Because we will adopt an $n = 3.3$ profile, the SMC halo velocity dispersion is larger than its stellar dispersion by $(3.3/2)^{1/2}$, implying that $\sigma_{\text{sat}}/\sigma_{\text{host}} = 3.3^{1/2} \sigma_{\text{SMC}}/v_{\text{rot}} = 0.21$. We adopt $\xi = 3$ based on typical orbits found by Kallivayalil et al. (2006), which yields $r_t = 0.107 D_{\text{SMC}} = 6.8$ kpc. Note, moreover, that at $\xi = 3$, $d \ln r_t / d \ln \xi \sim 0.24$, so the tidal radius is not very sensitive to the assumed properties of the orbit.

The most critical input to the likelihood calculation is the stellar density along the line of sight. Of course, images of the SMC give direct information only about its surface density as a function of position. One important clue to how the two are related comes from the HI velocity map of Stanimirović et al. (2004), which shows an inclined rotating disk with the receding side at a position angle of $\sim 60^\circ$ (north through east). This is similar to the $\sim 48^\circ$ position angle of the old-star optical profile found by Harris & Zaritsky (2006) based on data from Zaritsky et al. (2000). Hence, the spheroidal old-stellar population is closely aligned to the HI disk, although (as argued above) the stars in the SMC are pressure- rather than rotationally-supported. Our best clue to the line-of-sight profile is the major-axis profile exterior to the position of the source, which lies about 1 kpc to the southwest of the Galaxy center, roughly along the apparent major axis. The projected surface density is falling roughly as $r^{-2.3}$ over the ~ 1 kpc beyond the source position, from which we derive a deprojected exponent of $n = 3.3$. This is similar to the exponent for Milky Way halo stars. While there is a clear core in the star counts, this may be affected by crowding, and the core seems to have little impact on the counts beyond the source position (which is what is relevant to the density profile along the line of sight). Hence, we adopt $a_{\text{SMC}} = 1$ kpc.

The likelihood ratio is most sensitive to the assumptions made about the stellar density

in the outskirts of the SMC, hence to the power law and tidal radius adopted. This seems strange at first sight because the densities in these outlying regions are certainly extremely small, whatever their exact values. This apparent paradox can be understood as follows. For $D_{\text{LS}} \lesssim r_t$, the leading term in η is $\eta(D_{\text{LS}}) \sim [D_{\text{LS}}^2 + 4(b^2 + a_{\text{SMC}}^2)]^{-n/2}$, where $b = 1.0$ kpc is the impact parameter. In the outskirts, this implies $\eta(D_{\text{LS}}) \sim D_{\text{LS}}^{-n}$. The integrand in the numerator of equation (15) then scales as $\exp\{-[\Delta v(\mathbf{\Lambda}, D_{\text{LS}})]^2/4\sigma_{\text{SMC}}^2\} D_{\text{LS}}^{7/2-n}$. For fixed $\mathbf{\Lambda}$, Δv is a rising function of D_{LS} , and so for sufficiently large D_{LS} , the exponential will eventually cut off the integral. However, for the measured value of $\mathbf{\Lambda}$ (corresponding to $\Delta\tilde{v} \equiv |\mathbf{\Lambda}/\Lambda^2 - (\mathbf{v}_{\text{SMC}} - \mathbf{v}_{\odot})| \sim 300 \text{ km s}^{-1}$, the cutoff does not occur until $D_{\text{LS}} \sim (2\sigma_{\text{SMC}}/\tilde{v})D_{\text{SMC}} \sim 10$ kpc. Thus, as long as the density exponent remains $n \lesssim 3.5$ and as long as the density is not actually cut off by r_t , the integral keeps growing despite the very low density. On the other hand, a parallel analysis shows that the denominator in equation (15) is quite insensitive to assumptions about the outer parts of the SMC.

7.4. Likelihood Ratios

Using our adopted SMC parameters (eq. [17]), we find $\mathcal{L}_{\text{ratio}} \equiv \mathcal{L}_{\text{halo}}/\mathcal{L}_{\text{SMC}} = 27.4$. As discussed in § 7.3, this result is most sensitive to the outer SMC density profile, set by the exponent n and the cutoff r_t . If the tidal radius is increased from $r_t = 6.8$ kpc to $r_t = 10$ kpc and other parameters are held fixed, $\mathcal{L}_{\text{ratio}} = 30.3$. If the exponent is reduced from $n = 3.3$ to $n = 2.7$, then $\mathcal{L}_{\text{ratio}} = 29.1$. Hence, halo lensing is strongly favored in any case, but by an amount that would vary noticeably if any of our key model parameters were markedly off.

In carrying out these evaluations, we integrated equations (10) and (15) over all solutions with $\Delta\chi^2 < 9$. These solutions are grouped around three close-binary minima shown in Table 2. We carried out the integration in two different ways: over the discrete ensemble of solutions found by the Markov chains and uniformly over the three error ellipses that were fit to these chains. The results do not differ significantly. Figures 5 and 6 show $\mathbf{\Lambda}$ for the Markov-chain solutions superposed on likelihood contours for SMC and halo lenses respectively.

7.5. Kepler Constraints for Close Binaries

Binaries move in Kepler orbits. In principle, if we could measure all the Kepler parameters then these, together with the measured microlens parallax π_{E} (and the approximately known source distance D_{S}), would fix the mass and distance to the lens. While the two or-

bital parameters that we measure are not sufficient to determine the lens mass and distance, they do permit us to put constraints on these quantities.

Consider first the special case of a face-on binary in a circular orbit. Kepler’s Third Law implies that $GM/(br_E)^3 = \omega^2$ where M is the mass of the lens, b is the binary separation in units of the local Einstein radius r_E , and ω is the measured rotation parameter. Since $r_E = (D_{LS}/D_S)\tilde{r}_E$, this implies,

$$\frac{c^2}{4\tilde{r}_E b^3} \frac{D_S^2}{D_L D_{LS}^2} = \omega^2 \quad (\text{face – on circular}) \quad (19)$$

If one considers other orientations but remains restricted to face-on orbits, then this equation becomes a (“greater than”) inequality because at fixed projected separation, the apparent angular speed can only decrease.

Further relaxing to the case of non-circular orbits but with $\dot{b}/b = 0$ (i.e., the event takes place at pericenter), the rhs of equation (19) is halved, $\omega^2 \rightarrow \omega^2/2$, because escape speed (appropriate for near-parabolic orbits) is $\sqrt{2}$ larger than circular speed. Finally, after some algebra, and again working in the parabolic limit, one finds that including non-zero radial motion leads to $\omega^2/2 \rightarrow [\omega^2 + (\dot{b}/b)^2/4]/2$, and so to

$$\frac{D_L D_{LS}^2}{D_S^2} \leq \frac{c^2}{2\tilde{r}_E b^3} \left[\omega^2 + \frac{(\dot{b}/b)^2}{4} \right]^{-1}. \quad (20)$$

If the rhs of this equation is sufficiently small, then only lenses that are near the Sun ($D_L \ll D_S$) or near the SMC ($D_{LS} \ll D_S$) will satisfy it. In practice, we find that this places no constraint on SMC lenses, but does restrict halo lenses to be relatively close to the Sun, with the limit varying from ~ 2 kpc to ~ 10 kpc depending on the particular solution being probed and the MCMC realization of that solution. Integrating over the entire Markov chain, we find that $\mathcal{L}_{\text{ratio}}$ is reduced by a factor three, from 27.4 to 11.2.

7.6. Kepler Constraints for Wide Binaries

As discussed in § 6.1, all wide solutions are ruled out by their high χ^2 . Nevertheless, for completeness it is instructive to ask what sort of constraints could be put on the lens from measurement of the acceleration parameter α_b if these solutions had been accepted as viable. We rewrite equation (4) in terms of the parameter combination $T \equiv (\pi_E \gamma / \alpha_b)^{1/2}$, which has units of time,

$$\sqrt{\frac{D_L}{60 \text{ kpc}} \frac{D_{LS}}{D_S}} = \frac{cT}{2} \sqrt{\frac{\sin^3 i}{60 \text{ kpc AU}}} < 0.28 \frac{T}{\text{yr}}. \quad (21)$$

The five wide-binary zero-blending solutions listed in Table 2 have, respectively, $T = (0.039, 0.032, 0.035, 0.017, 0.015)$ yr. Thus, if these solutions had been viable, the lens would have been firmly located in the SMC (or else, improbably, within 6 pc of the Sun). This demonstrates the power of this constraint for wide binaries, which derives from light-curve features that arise from the motion of the center of magnification relative to the center of mass. These obviously do not apply to close binaries for which the center of magnification is identical to the center of mass.

However, this same relative motion makes it *more difficult* to constrain the nature of the lens from measurements of the projected velocity, $\tilde{\mathbf{v}}$. This is because the parallax measurement directly yields only the projected velocity of the center of magnification, whereas models of the lens populations constrain the motion of the center of mass. If \dot{b} is measured, it is straight forward to determine the component of the difference between these two that is parallel to the binary axis, namely

$$\Delta\tilde{v}_{\parallel} = \frac{\dot{b}}{1+q} \frac{\text{AU}}{\pi_{\text{E}}}. \quad (22)$$

On the other hand, the measurement of α_b indicates that there is motion in the transverse direction, but specifies neither the amplitude nor sign. For example, for circular motion with the line of nodes perpendicular to the binary axis,

$$\Delta\tilde{v}_{\perp} = \pm \sqrt{\frac{\alpha_b b}{1+q}} \frac{\text{AU}}{\pi_{\text{E}}} \csc i, \quad (23)$$

and hence,

$$\frac{\Delta\tilde{v}_{\perp}}{\tilde{v}} = \pm \sqrt{\frac{\alpha_b b}{1+q}} t_{\text{E}} \csc i, \quad (24)$$

If this ratio (modulo the $\csc i$ term) is small, then the internal motion can be ignored (assuming the inclination is not unluckily low). In the present case, the quantity $[\alpha_b b / (1+q)]^{1/2} t_{\text{E}}$ for the five respective wide-binary solutions shown in Table 2 is (0.23, 0.36, 0.25, 1.04, 0.77), implying that constraints arising from measurement of \tilde{v} would be significantly weakened.

Again, however, since the wide solutions are in fact ruled out, all of these results are of interest only for purposes of illustration.

7.7. Constraints From (Lack of) Finite-Source Effects

Finite source effects are parameterized by $\rho \equiv \theta_*/\theta_{\text{E}}$, where θ_* is the angular size of the source. Equivalently, $\rho = (D_{\text{L}}/D_{\text{LS}})(r_*/\tilde{r}_{\text{E}})$, where $r_* = D_{\text{S}}\theta_*$ is the physical source radius.

Since the source is a clump giant, with $r_* \sim 0.05$ AU, this implies

$$\rho = 0.021 \frac{D_L}{60 \text{ kpc}} \frac{5 \text{ kpc}}{D_{\text{LS}}} \frac{\pi_E}{0.035} \quad (25)$$

All models described above assume $\rho = 0$. Since the impact parameter is $u_0 \sim 0.08$ and the semi-diameter of the caustic is $2Q \sim 0.02$, finite source effects should be pronounced for $\rho \gtrsim u_0 - 2Q \sim 0.06$. In fact, we find that zero-blending models with $\rho \lesssim 0.05$ are contraindicated by $\Delta\chi^2 \sim (\rho/0.0196)^4$. This further militates against SMC lenses, which predict acceptable values of ρ only for relatively large source-lens separations. If we penalize solutions with finite source effects by $\Delta\chi^2 = (\rho/0.0196)^2$, we find that $\mathcal{L}_{\text{ratio}}$ rises from 11.2 to 20.3.

8. Discussion

By combining ground-based and *Spitzer* data, we have measured the microlensing parallax accurate to 0.003 units, by far the best parallax measurement yet for an event seen toward the Magellanic Clouds. Our analysis significantly favors a halo location for the lens over SMC self lensing. It excludes altogether lensing by Galactic disk stars. Of course, with only one event analyzed using this technique, an SMC location cannot be absolutely excluded based on the $\sim 5\%$ probability that we have derived. The technique must be applied to more events before firm conclusions can be drawn. *Spitzer* itself could be applied to this task. Even better would be observations by the *Space Interferometry Mission (SIM)* (Gould & Salim 1999), for which time is already allocated for 5 Magellanic Cloud events. *SIM* would measure both π_E and θ_E and so determine (rather than statistically constrain) the position of the lens.

Assuming that the lens is in the halo, what are its likely properties? The mass is

$$M = 10.0 M_\odot \left(\frac{\pi_E}{0.047} \right)^{-2} \frac{\pi_{\text{rel}}}{180 \mu\text{as}}, \quad (26)$$

where the fiducial π_E is the best-fit value and the fiducial π_{rel} is for a “typical” halo lens, which (after taking account of the constraint developed in § 7.5) would lie at about 5 kpc. In the best-fit model, the mass ratio is $q = 2.77$, which would imply primary and secondary masses of 7.3 and 2.7 M_\odot respectively. The projected separation would be $b = 0.22$ Einstein radii, i.e., 4.7 AU (D_{LS}/D_S). Note that at these relatively close distances, main-sequence stars in this mass range would shine far too brightly to be compatible with the strict constraints on blended light. Hence, the lenses would have to be black holes.

We must emphasize that the test carried out here *uses only kinematic attributes* of the lens populations and assumes no prior information about *their mass functions*. Note, in

particular, that if we were to adopt as a prior the lens mass distribution inferred by the MACHO experiment (Alcock et al. 2000), then the MACHO hypothesis would be strongly excluded. Recall from § 7.5 (eq. [20]), that the lens is either very close to the SMC or within 10 kpc of the Sun. However, from equation (26), for $D_L < 10$ kpc, we have $M \lesssim 4.6 M_\odot$, and hence a primary mass $Mq/(1+q) \lesssim 3.4 M_\odot$. From Figures 12–14 of Alcock et al. (2000), such masses are strongly excluded as the generators of the microlensing events they observed toward the LMC.

Hence, if the MACHO hypothesis favored by this single event is correct, the MACHO population must have substantially different characteristics from those inferred by Alcock et al. (2000), in particular, as mentioned above, a mass scale of order $10 M_\odot$ or perhaps more. Alcock et al. (2001a) limit the halo fraction of such objects to $< 30\%$ at $M = 10 M_\odot$ and to $< 100\%$ at $M = 30 M_\odot$. At higher masses, the sensitivity of microlensing surveys deteriorates drastically. However, Yoo et al. (2004) derived important limits in this mass range from the distribution of wide binaries in the stellar halo, putting an upper limit at 100% for $M = 40 M_\odot$ and at 20% for $M > 200 M_\odot$. Thus, if the MACHO hypothesis is ultimately confirmed, this would be a new population in the mass “window” identified in Figure 7 of Yoo et al. (2004) between the limits set by microlensing and wide-binary surveys. This again argues for the importance of obtaining space-based parallaxes on additional microlensing events.

As we discussed in some detail in § 7.3 (particularly the last paragraph) our conclusion regarding the relatively low probability of the lens being in the SMC rests critically on the assumption that the SMC lens population falls off relatively rapidly along the line of sight. (We adopted an $n = 3.3$ power law.) This is because equation (16) scales $\propto D_{LS}^{7/2-n}$. If the SMC had a halo lens population with a much shallower falloff than we have assumed, this term could dominate the integral in equation (15) even if the overall normalization of the halo were relatively low. Hence, Magellanic Cloud halo lensing could provide an alternate explanation both for this SMC event and the events seen by MACHO toward the LMC. As mentioned above, *SIM* could easily distinguish between this conjecture and the halo-lens hypothesis.

Finally, we remark that analysis of this event was extraordinarily difficult because it was a “weak” (i.e., non-caustic-crossing) binary. If it had been either a single-mass lens or a caustic-crossing binary, it would have been much easier to analyze and the inferences regarding its location (in the halo or the SMC) would have been much more transparent. We therefore look forward to applying this same technique to more typical events.

We thank Scott Gaudi for a careful reading of the manuscript, which led to many

useful suggestions. We are also grateful to Patrick Tisserand for his comments. S.D. and A.G. were supported in part by grant AST 042758 from the NSF. Support for OGLE was provided by Polish MNiSW grant N20303032/4275, NSF grant AST-0607070 and NASA grant NNG06GE27G. Any opinions, findings, and conclusions or recommendations expressed in this material are those of the authors and do not necessarily reflect the views of the NSF.

REFERENCES

- Afonso, C. et al. 2003, *A&A*, 400, 951
- Albrow, M.D. et al. 1999, *ApJ*, 522, 1022
- Albrow, M.D. et al. 2000, *ApJ*, 534, 894
- Alcock, C. et al. 1993, *Nature*, 365, 621
- Alcock, C. et al. 1995, *ApJ*, 454, L125
- Alcock, C. et al. 1997, *ApJ*, 491, 436
- Alcock, C. et al. 2000, *ApJ*, 542, 281
- Alcock, C. et al. 2001, *Nature*, 414, 617
- Alcock, C. et al. 2001, *ApJ*, 550, L169
- An, J.H. et al. 2005, *MNRAS*, 356, 1409
- An, J.H. et al. 2002, *ApJ*, 572, 521
- Assef, R.J. et al., 2006, *ApJ*, in press (astro-ph/0604147)
- Aubourg, E. et al. 1993, *Nature*, 365, 623
- Boutreux, T. & Gould, A. 1996, *ApJ*, 462, 705
- Chang, K. & Refsdal, S. 1979, *Nature*, 282, 561
- Chang, K. & Refsdal, S. 1984, *A&A*, 130, 157
- Dominik, M. 1999, *A&A*, 349, 108
- Doran, M., & Mueller, C.M. 2003, *ArXiv Astrophysics e-prints*, arXiv:astro-ph/0311311
- Jiang, G. et al. 2005, *ApJ*, 615, 450
- Gould, A. 1994, *ApJ*, 421, L75
- Gould, A. 1995, *ApJ*, 441, L21
- Gould, A. 1999, *ApJ*, 514, 869
- Gould, A. 2004, *ApJ*, 606, 319

- Gould, A., Bennett, D.P., & Alves, D.R. 2004, ApJ, 614, 404
- Gould, A., Miralda-Escudé & Bahcall, J.N. 1994, ApJ, 423, L105
- Gould, A. & Salim, S. 1999 ApJ, 524, 794
- Harris, J. & Zaritsky, D. 2006, AJ, 131, 2514
- Jiang, G. et al. 2005, ApJ, 617, 1307
- Kallivayalil, N., van der Marel, R.P., & Alcock, C. 2006, ApJ, in press, astro-ph/0606240
, King, I. 1962, AJ, 67, 471
- Paczynski, B. 1986, ApJ, 304, 1
- Park, B.-G. et al. 2004, ApJ, 609, 166
- Poindexter, S., Afonso, C., Bennett, D.P., Glicenstein, J.-F., Gould, A. Szymański, M., & Udalski, A. 2005, ApJ, 633, 914
- Reach, W. T., et al. 2005, PASP, 117, 978
- Read, J.I., Wilkinson, M.I., Evans, N.W., Gilmore, G., Kleyna, J.T. 2006, MNRAS, 366, 429
- Refsdal, S. 1966, MNRAS, 134, 315
- Smith, M., Mao, S., & Paczynski, B. 2003, MNRAS 339, 925
- Stanimirović, S. Staveley-Smith, L., & Jones, P.A. ApJ, 604, 176
- Tisserand, P. et al. 2006, A&A, submitted (astro-ph/0607207)
- Udalski, A. 2003, Acta Astron., 53, 291
- Woźniak, P.R. 2000, Acta Astron., 50, 421
- Yoo, J., Chanamé, J., & Gould, A. 2004, ApJ, 601, 311
- Zaritsky, D., Harris, J., Grebel, E.K., & Thompson, I.B. 2000, ApJ, 534, L53

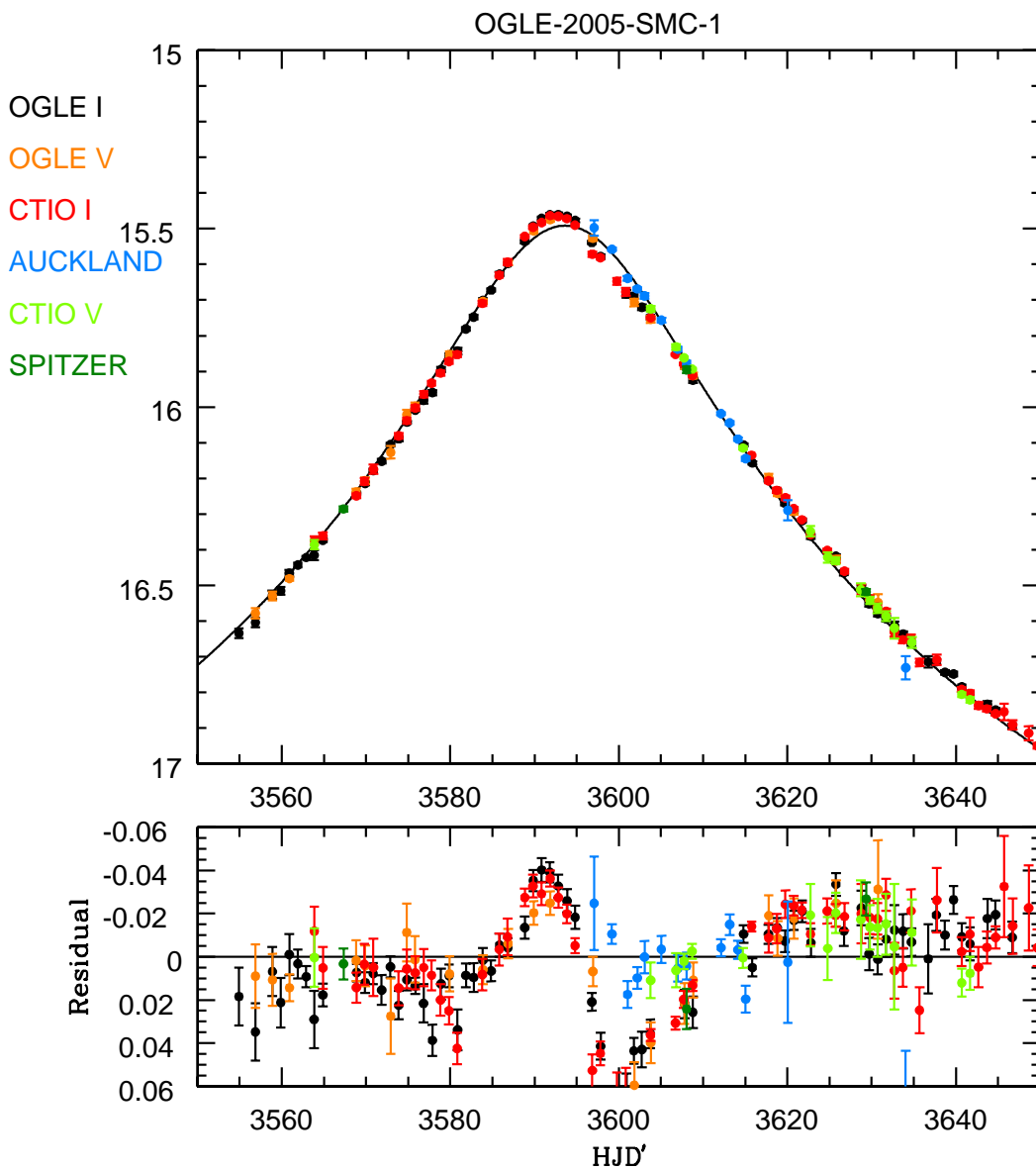


Fig. 1.— Standard (Paczynski 1986) microlensing fit to the light curve of OGLE-2005-SMC-001, with data from OGLE *I* and *V* in Chile, μ FUN *I* and *V* in Chile, Auckland clear-filter in New Zealand, and the *Spitzer* satellite $3.6 \mu\text{m}$ at ~ 0.2 AU from Earth. The data are binned by the day. All data are photometrically aligned with the (approximately calibrated) OGLE data. The residuals are severe indicating that substantial physical effects are not being modeled. The models do not include parallax, but when parallax is included, the resulting figure is essentially identical.

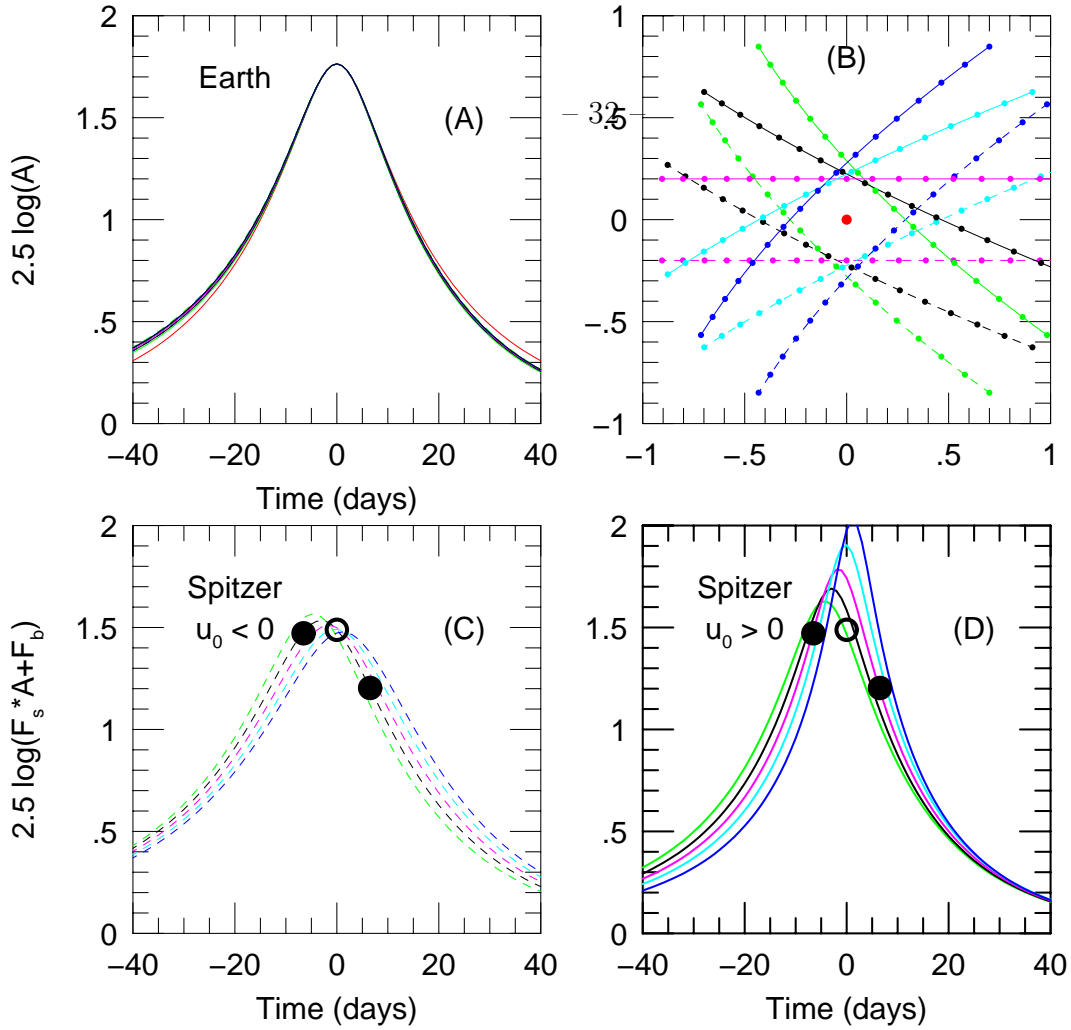


Fig. 2.— Why 4 (not 3) *Spitzer* observations are needed to measure $\boldsymbol{\pi}_E = (\pi_{E,\parallel}, \pi_{E,\perp})$. Panel A shows Earth-based light curve of hypothetical event (*black curve*) with $\boldsymbol{\pi}_E = (0.4, -0.2)$, $u_0 = -0.2$, and $t_E = 40$ days, together with the corresponding (*red*) lightcurve with zero parallax. From the asymmetry of the lightcurve, one can measure $\pi_{E,\parallel} = 0.4$ and $|u_0| = 0.2$, but no information can be extracted about $\pi_{E,\perp}$ or the sign of u_0 . Indeed, 9 other curves are shown with various values of these parameters, and all are degenerate with the black curve. Panel (B) shows the trajectories of all ten models in the geocentric frame (Gould 2004) that generate these degenerate curves. *Solid* and *dashed* curves indicate positive and negative u_0 , respectively, with $\pi_{E,\perp} = -0.4, -0.2, 0, +0.2, +0.4$ (*green, black, magenta, cyan, blue*). Motion is toward positive x , while the Sun lies directly toward negative x . Dots indicate 5 day intervals. Panel C shows full light curves as would be seen by *Spitzer*, located 0.2 AU from the Earth at a projected angle 60° from the Sun, for the 5 $u_0 < 0$ trajectories in Panel B. The source flux F_s and blended flux F_b are fit from the two *filled circles* and a third point at baseline (not shown) as advocated by Gould (1999). Note that these two points (plus baseline) pick out the “true” (*black*) trajectory, from among other solutions that are consistent with the ground-based data with $u_0 < 0$, but Panel D shows that these points alone would pick out the *magenta* trajectory among $u_0 > 0$ solutions, which has a different $\pi_{E,\perp}$ from the “true” solution. However, a fourth measurement *open circle* would rule out this *magenta* $u_0 > 0$ curve and so confirm the *black* $u_0 < 0$ curve.

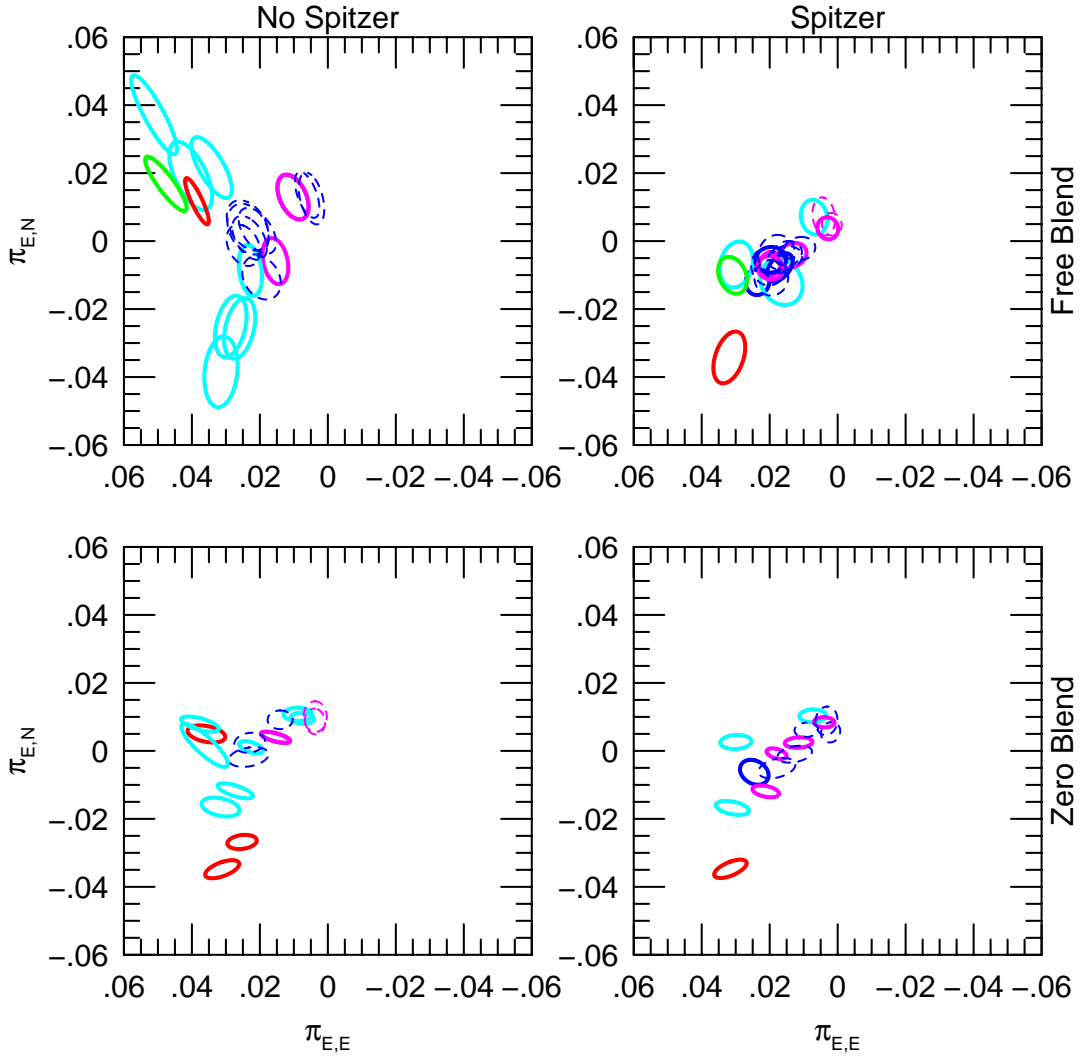


Fig. 3.— Parallax $\boldsymbol{\pi}_E = (\pi_{E,N}, \pi_{E,E})$ 1σ error ellipses for all discrete solutions for OGLE-2005-SMC-001. The left-hand panels show fits excluding the *Spitzer* data, while the right-hand panels include these data. The upper panels show fits with blending as a free parameter whereas the lower panels fix the OGLE blending at zero. The ellipses are coded by $\Delta\chi^2$ (relative to each global minimum), with $\Delta\chi^2 < 1$ (red), $1 < \Delta\chi^2 < 4$ (green), $4 < \Delta\chi^2 < 9$ (cyan), $9 < \Delta\chi^2 < 16$ (magenta), $\Delta\chi^2 > 16$ (blue). Close- and wide-binary solutions are represented by bold and dashed curves, respectively. Most of the “free-blend, no-*Spitzer*” solutions are highly degenerate along the $\pi_{E,\perp}$ direction (33° north through east), as predicted from theory, because only the orthogonal ($\pi_{E,\parallel}$) direction is well constrained from ground-based data. As seen from the two upper panels, the *Spitzer* observations reduce the errors in the $\pi_{E,\perp}$ direction by a factor ~ 3 when the blending is a free parameter. However, fixing the blending (lower panels) already removes this freedom, so *Spitzer* observations then have only a modest additional effect.

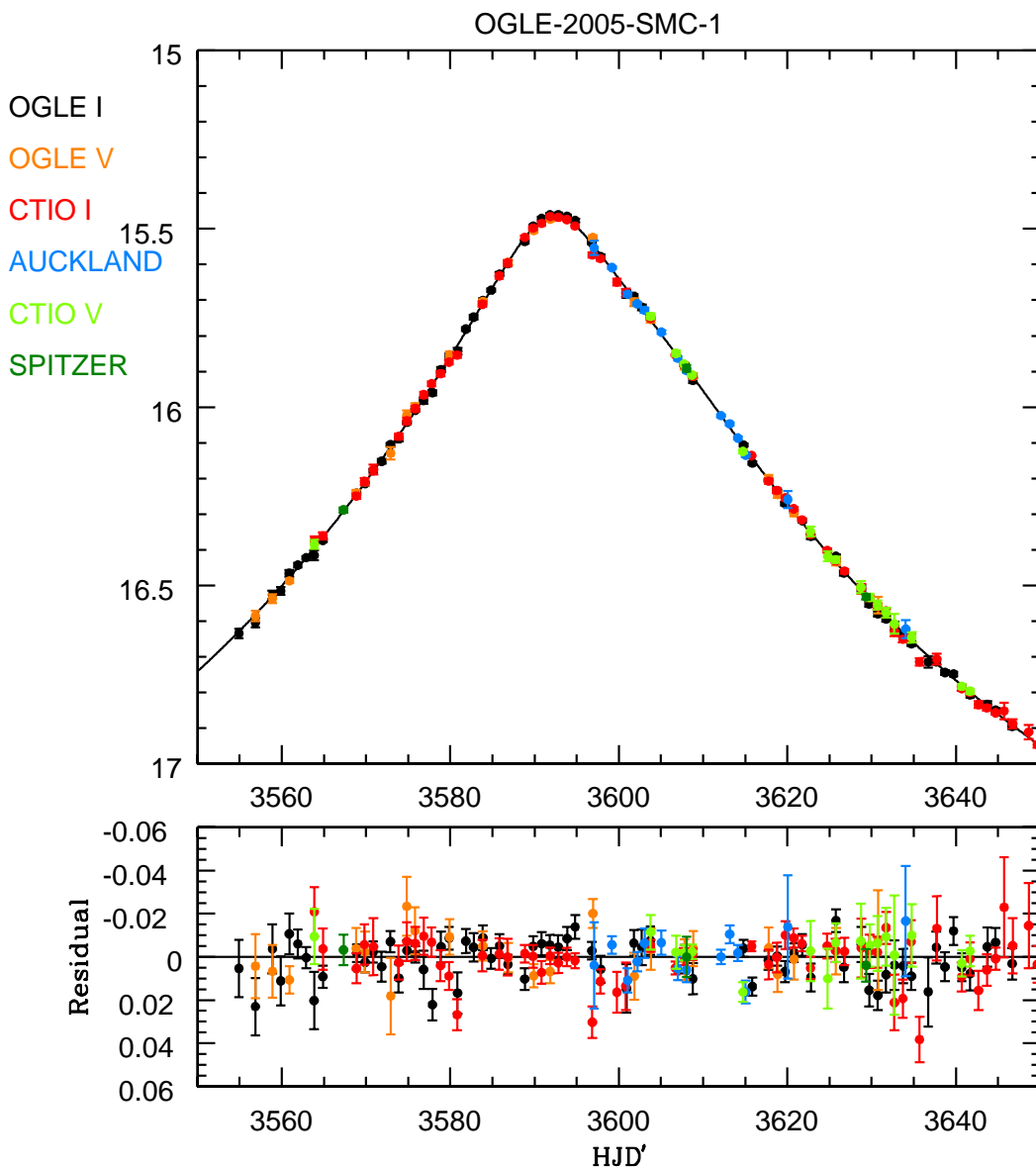


Fig. 4.— Best-fit binary microlensing model for OGLE-2005-SMC-001 together with the same data shown in Fig. 1. The model includes microlens parallax (2 parameters) and binary rotation (2 parameters). All data are photometrically aligned with the (approximately calibrated) OGLE data, and the *Spitzer* data are further adjusted to take account of the different magnification pattern at their location (given the microlens parallax of the model). The residuals show no major systematic trends.

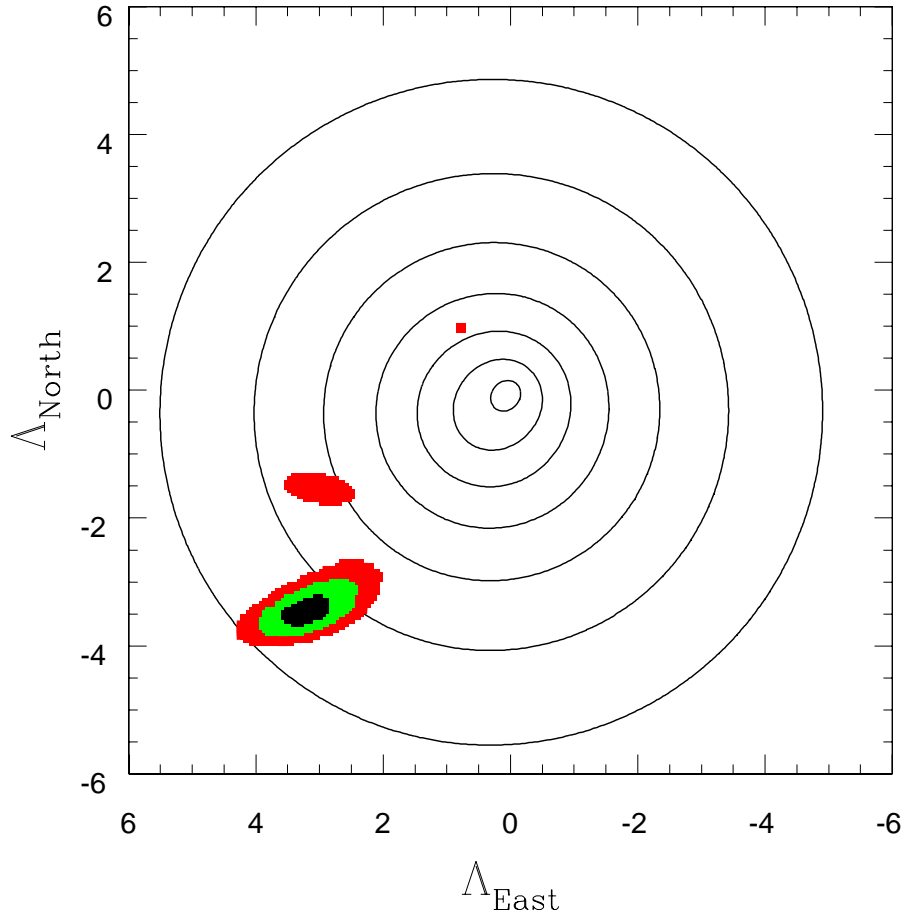


Fig. 5.— Likelihood contours of the inverse projected velocity $\mathbf{\Lambda} \equiv \tilde{\mathbf{v}}/\tilde{v}^2$ for SMC lenses together with $\mathbf{\Lambda}$ values for light-curve solutions found by Monte Carlo Markov chain. The latter are color-coded for solutions with $\Delta\chi^2$ within 1, 4, and 9 of the global minimum. The likelihood contours are spaced by factors of 5.

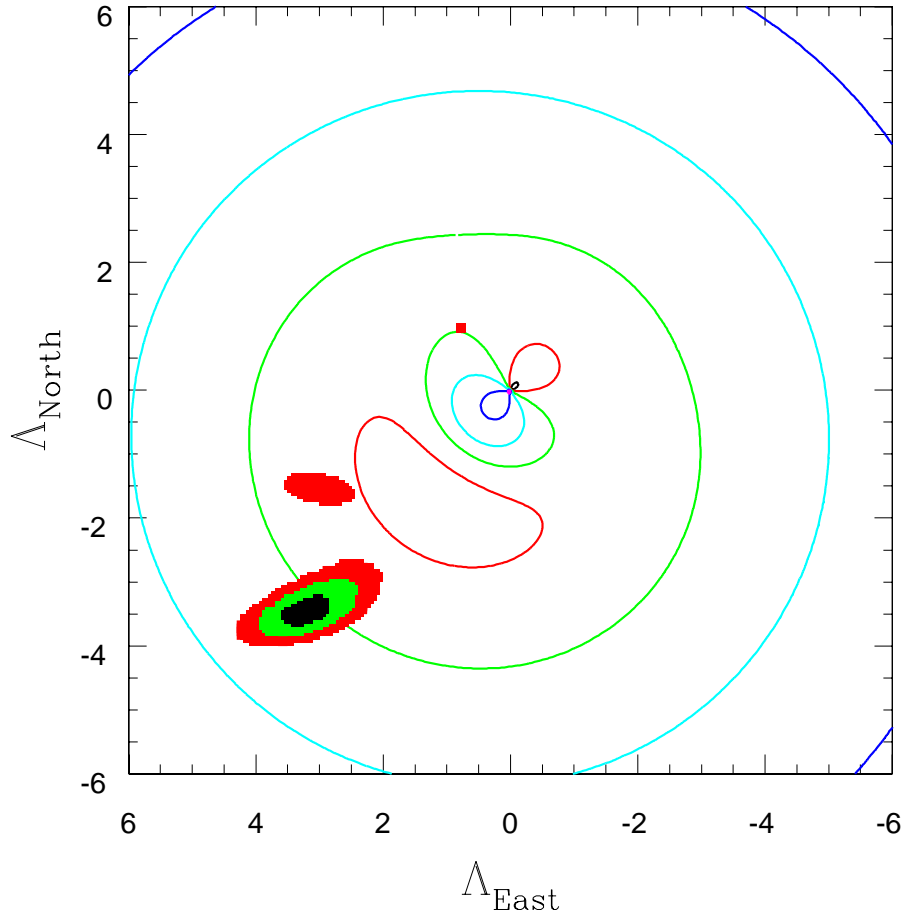


Fig. 6.— Likelihood contours of the inverse projected velocity $\Lambda \equiv \tilde{\mathbf{v}}/\tilde{v}^2$ for halo lenses together with Λ values for light-curve solutions found by Monte Carlo Markov chain. Similar to Figure 5 except in this case the contours are color coded, with black, red, yellow, green, cyan, blue, magenta, going from highest to lowest.

Table 1. Light Curve Models: Free Blending.

Model χ^2	t_0 (day)	u_0 ($\times 100$)	t_E (day)	q	$Q : \gamma$ ($\times 100$)	ϕ (deg)	$\pi_{E,N}$	$\pi_{E,E}$	$\omega : \alpha_b^{1/2}$ (yr^{-1})	\dot{b}/b (yr^{-1})	F_b/F_{base}
C- a 1455.40	3593.751 0.040	-8.729 0.532	174.17 8.13	2.77 0.33	0.980 0.066	21.70 1.10	-0.0342 0.0076	0.0319 0.0047	0.073 0.047	5.60 0.46	0.003 0.061
C+ a	3593.687 1475.74	7.763 0.033	190.03 6.58	2.15 0.26	0.850 0.046	19.34 1.26	-0.0120 0.0039	0.0236 0.0035	-0.141 0.027	5.83 0.48	0.115 0.040
C- b 1462.89	3593.560 0.036	-9.567 0.509	160.61 6.69	0.98 0.25	0.999 0.063	9.23 1.89	-0.0069 0.0068	0.0298 0.0049	0.331 0.032	0.40 0.61	-0.101 0.060
C+ b	3593.643 1466.84	9.321 0.040	163.41 4.52	1.11 0.15	1.002 0.046	11.24 1.12	-0.0068 0.0036	0.0199 0.0032	-0.167 0.029	1.33 0.26	-0.071 0.040
C- c 1463.52	3593.473 0.042	-9.020 0.352	171.06 5.89	0.29 0.04	0.837 0.041	-3.34 1.31	0.0070 0.0051	0.0069 0.0039	0.746 0.069	-3.87 0.44	-0.030 0.043
C+ c	3593.460 1465.15	9.207 0.042	167.46 4.15	0.29 0.03	0.853 0.035	-3.78 1.24	0.0038 0.0032	0.0029 0.0031	-0.743 0.070	-3.92 0.41	-0.053 0.033
C- d 1464.13	3593.639 0.058	-9.831 0.480	157.29 6.18	0.90 0.15	1.052 0.062	8.53 1.18	-0.0121 0.0067	0.0166 0.0062	0.146 0.096	-0.04 0.27	-0.131 0.057
C+ d	3593.676 1467.70	9.406 0.056	162.74 4.42	0.79 0.14	1.001 0.043	7.86 1.47	-0.0042 0.0036	0.0135 0.0043	-0.144 0.048	-0.12 0.50	-0.080 0.040
C+ e	3593.655 1474.32	9.161 0.047	165.60 7.24	1.10 0.20	0.983 0.060	11.36 1.42	-0.0055 0.0038	0.0197 0.0045	-0.162 0.038	1.50 0.74	-0.051 0.058
C+ f	3593.769 1474.40	7.516 0.038	194.33 7.10	1.86 0.33	0.826 0.048	19.21 1.46	-0.0078 0.0042	0.0170 0.0038	-0.018 0.041	5.94 0.72	0.140 0.042
C-⊥a 1457.55	3593.251 0.030	-8.026 0.370	176.25 6.94	1.74 0.20	0.719 0.041	280.21 0.53	-0.0101 0.0054	0.0309 0.0043	0.758 0.049	1.10 0.34	0.061 0.046
C+⊥a	3593.272 1470.74	7.900 0.035	177.32 5.33	1.40 0.25	0.752 0.052	280.03 0.58	-0.0079 0.0035	0.0198 0.0038	-0.599 0.084	1.45 0.32	0.073 0.037
W- a	3593.708 1471.32	-8.470 0.037	170.22 5.70	2.49 0.40	0.936 0.036	6.38 0.51	0.0073 0.0056	0.0041 0.0033	0.241 0.175	0.49 0.02	-0.004 0.038
W+ a	3593.703 1471.29	8.568 0.035	167.72 4.70	2.48 0.40	0.950 0.034	6.37 0.49	0.0050 0.0033	0.0017 0.0029	0.273 0.174	0.49 0.02	-0.016 0.033
W-⊥a	3593.562 1474.79	-8.666 0.067	174.41 6.31	2.28 1.03	1.154 0.048	279.74 0.61	-0.0039 0.0057	0.0180 0.0054	0.841 0.385	-0.75 0.06	0.009 0.043
W+⊥a	3593.641 1480.79	9.281 0.062	165.12 4.04	7.39 5.71	1.158 0.048	279.74 0.60	-0.0036 0.0036	0.0148 0.0042	0.804 0.339	-0.23 0.18	-0.060 0.034
W-⊥b	3593.570 1475.50	-9.209 0.062	166.04 5.83	3.21 1.92	1.207 0.053	279.24 0.58	-0.0074 0.0056	0.0204 0.0051	0.909 0.360	-0.16 0.18	-0.054 0.046
W+⊥b	3593.659 1480.16	8.897 0.068	171.08 3.89	5.28 3.53	1.125 0.042	280.32 0.61	-0.0023 0.0035	0.0112 0.0046	0.826 0.305	-0.77 0.06	-0.016 0.030
W-⊥c	3593.492 1474.90	-9.443 0.046	163.30 5.24	2.20 0.51	1.291 0.052	278.45 0.48	-0.0108 0.0053	0.0195 0.0050	1.094 0.244	0.49 0.05	-0.086 0.040
W+⊥c	3593.534 1486.02	9.492 0.049	162.68 3.70	2.96 0.69	1.267 0.043	278.50 0.49	-0.0050 0.0035	0.0155 0.0051	1.054 0.252	0.44 0.05	-0.091 0.030

Table 2. Light Curve Models: Zero Blending.

Model χ^2	t_0 (day)	u_0 ($\times 100$)	t_E (day)	q	$Q : \gamma$ ($\times 100$)	ϕ (deg)	$\pi_{E,N}$	$\pi_{E,E}$	$\omega : \alpha_b^{1/2}$ (yr^{-1})	\dot{b}/b (yr^{-1})
C- a 1455.38	3593.751 0.039	-8.755 0.028	173.72 0.88	2.77 0.32	0.984 0.018	21.69 1.15	-0.0347 0.0027	0.0316 0.0048	0.075 0.047	5.59 0.29
C+ a 1474.91	3593.648 0.041	8.728 0.025	171.75 0.58	1.42 0.24	0.940 0.019	14.45 1.51	-0.0063 0.0037	0.0245 0.0042	-0.191 0.039	3.21 0.59
C- b 1463.48	3593.612 0.028	-8.708 0.020	173.51 0.48	0.85 0.18	0.898 0.017	9.17 1.68	0.0026 0.0021	0.0300 0.0046	0.368 0.030	1.04 0.59
C+ b 1469.51	3593.687 0.034	8.711 0.021	172.11 0.45	0.93 0.11	0.924 0.016	10.57 1.08	-0.0008 0.0016	0.0180 0.0030	-0.172 0.028	1.39 0.29
C- c 1464.10	3593.488 0.038	-8.769 0.023	175.52 0.63	0.28 0.03	0.813 0.017	-3.31 1.34	0.0103 0.0019	0.0074 0.0039	0.753 0.062	-3.89 0.47
C+ c 1467.54	3593.493 0.038	8.770 0.023	174.27 0.67	0.27 0.03	0.809 0.017	-3.67 1.22	0.0084 0.0015	0.0040 0.0030	-0.735 0.065	-3.88 0.43
C+ d 1470.98	3593.751 0.051	8.725 0.027	172.80 0.50	0.65 0.10	0.919 0.015	7.20 1.47	0.0025 0.0015	0.0115 0.0041	-0.137 0.047	-0.11 0.55
C-⊥a 1460.01	3593.233 0.031	-8.524 0.019	166.86 0.49	1.77 0.23	0.762 0.030	279.76 0.48	-0.0168 0.0020	0.0310 0.0049	0.746 0.055	0.73 0.25
C+⊥a 1470.98	3593.269 0.032	8.524 0.019	166.68 0.50	1.56 0.25	0.799 0.034	279.87 0.49	-0.0119 0.0017	0.0211 0.0039	-0.597 0.058	0.73 0.22
W+ a 1479.54	3593.590 0.059	8.522 0.020	167.60 0.46	8.33 6.18	0.953 0.016	8.38 0.78	0.0062 0.0021	0.0092 0.0035	0.267 0.161	-0.21 0.20
W- a 1471.40	3593.718 0.033	-8.449 0.040	170.56 0.71	2.40 0.38	0.937 0.014	6.51 0.44	0.0088 0.0042	0.0033 0.0032	0.296 0.175	0.49 0.02
W+ b 1471.49	3593.709 0.034	8.427 0.037	170.01 0.90	2.41 0.37	0.931 0.014	6.54 0.44	0.0055 0.0030	0.0021 0.0028	0.210 0.163	0.50 0.02
W-⊥a 1474.83	3593.552 0.067	-8.742 0.028	173.11 1.11	2.20 0.97	1.169 0.038	279.61 0.59	-0.0051 0.0030	0.0179 0.0055	0.880 0.398	-0.73 0.25
W+⊥a 1480.41	3593.642 0.069	8.759 0.025	172.88 1.15	4.51 2.76	1.115 0.036	280.27 0.62	-0.0010 0.0025	0.0126 0.0051	0.769 0.359	-0.76 0.21